Journal of Constructional Steel Research 212 (2024) 108248

Contents lists available at ScienceDirect

Journal of Constructional Steel Research

journal homepage: www.elsevier.com/locate/jcsr

Determining the seismic performance factors of quasi-X bracing systems

Alireza Shirpour, Nader Fanaie *

Department of Civil Engineering, K. N. Toosi University of Technology, Tehran, Iran

ARTICLE INFO

Keywords:
Quasi-X bracing systems
Seismic performance factors (SPFs)
FEMA P695 approach
Far-field ground motion (FFGM) records
Non-linear static (pushover) analysis
Incremental dynamic analysis (IDA)

ABSTRACT

This paper proposes two novel quasi-X bracing systems to resolve the drawbacks of concentrically braced frames (CBFs) and enhance their ductility. The seismic performance factors (SPFs) for moment-resisting frames equipped with these braces are determined according to the FEMA P695 approach. In pursuit of this aim, a three-dimensional set of 2-, 4-, 6-, and 8-story archetypes in two separate seismic design categories (SDC C_{max} and C_{min}) were designed considering presumed SPFs. Initially, non-linear static (pushover) analysis was carried out on each of the archetypes, and their period-based ductility and over-strength factors were extracted. Afterward, the archetypes' seismic performance was evaluated by performing incremental dynamic analysis (IDA) under far-field ground motion (FFGM) records, and the accuracy of the presumed response modification factor was examined as per FEMA P695. Based on the obtained results, a response modification factor of 5 is deemed acceptable for the design of both quasi-X bracing systems. Furthermore, the values of the deflection amplification factor and the over-strength factor are acquired as 5 and 3, respectively.

1. Introduction

Concentrically braced frames (CBFs) are regarded as one of the most commonly employed components for ensuring lateral resistance in structures. Due to their high stiffness, minimal lateral displacement, ease of implementation, and cost-effectiveness, these systems have invariably encouraged steel structure designers to utilize them. One of the significant drawbacks of this bracing system is its limited ductility due to the buckling of bracing members prior to yielding. Achieving an appropriate combination of stiffness and ductility in this common bracing system can effectively mitigate this drawback [1–3]. Extensive research and studies have been conducted in the past two decades to enhance the ductility of CBFs. In each of these studies, endeavors have been made to improve the ductility of these bracing systems by modifying connections or incorporating a ductility element [4–8]. One of the most appropriate and effective approaches for enhancing ductility and energy dissipation in CBFs is the utilization of yielding dampers at their center. During severe earthquakes, these yielding dampers act as fuses and prevent damage to the main structural members. Yielding damped braced frames (YDBFs) were initially invented by Tyler and subsequently developed by Jurokovski [9,10]. Ciampi and Ferretti have evaluated two distinct YDBFs [11]. Along with examining the Marsh and Pall systems [12], Vulcano [13] furthered the research conducted by Ciampi et al. on YDBFs [14,15]. Sabouri and Roufegarinejad examined the hysteresis behavior of YDBFs with different opening percentages [16]. In order to improve the seismic performance of cross-braced frames by utilizing the concept of bending steel plates for energy absorption, Payandehjoo et al. have presented the drawer bracing system (DBS) [17]. Afterward, researchers realized that utilizing a circular ring constructed from tubular cross-sections enhances the resistance of YDBFs. The nearly uniform yielding in circular dampers enables the utilization of the entire cross-sectional capacity for energy absorption and resistance [18,19].

Trombetti et al. presented a novel bracing system called the crescent-shaped brace (CSB) to effectively tackle the CBF systems' buckling issue. Their research revealed that this innovative system exhibits remarkable potential in achieving numerous seismic design purposes, including stiffness, strength, and ductility [20]. Palermo et al. carried out comprehensive experimental investigations on CSB systems. Their studies demonstrated that the initial lateral stiffness and yield strength are decoupled, operating independently. Furthermore, these braces possess a substantial capacity for ultimate hardening and ductility, effectively mitigating the risk of failure attributed to second-order effects [21–23]. The geometric shape of these braces not only leads to enhanced energy dissipation but also provides the ability to set the desired stiffness level. In addition, they found that CSBs, owing to their stable cyclic performance and energy dissipation capabilities without

* Corresponding author at: K. N. Toosi University of Technology, Civil Engineering Department, No. 1346, Vali-Asr Street, P.O. Box. 15875-4416, 19697 Tehran, Iran.
E-mail address: fanaie@kntu.ac.ir (N. Fanaie).

https://doi.org/10.1016/j.jcsr.2023.108248
Received 20 July 2023; Received in revised form 10 September 2023; Accepted 25 September 2023
Available online 5 October 2023

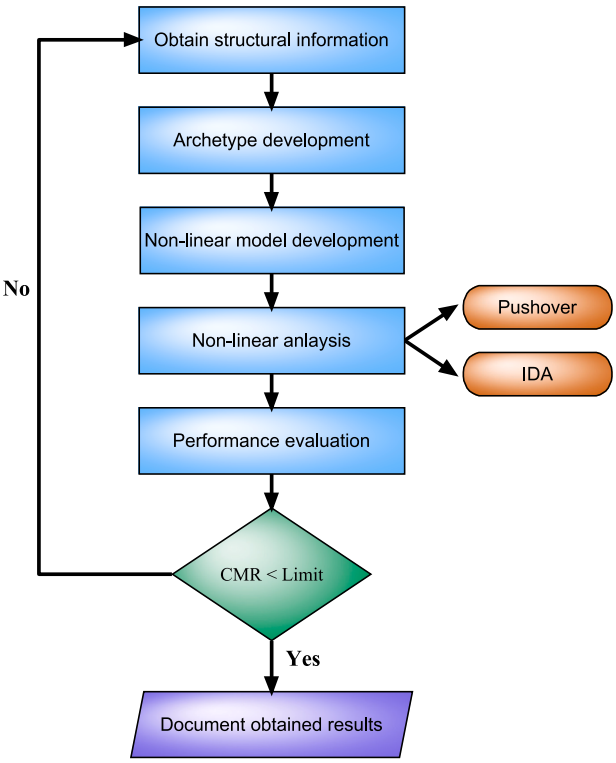

Fig. 1. Flowchart of FEMA P695 guideline [36].

declining strength and stiffness degradation, can serve as a viable alternative to buckling restrained braces (BRBs) [24,25]. In recent years, the circular-shaped brace (OGrid) has been presented by Boostani et al., and the elliptical-shaped brace has been introduced by Jonghani et al. Both of these bracing systems underwent comprehensive evaluations through experimental and numerical studies. The obtained outcomes revealed that despite having appropriate stiffness and ductility, the connection of the bracing members to the columns in these two bracing systems leads to the formation of a plastic hinge at the middle of the column [26–28]. Shamivand and Akbari proposed the Shami lateral bracing system (SLB), a novel ring-shaped brace that rectifies the issue of brace-to-main column connections by employing quasi-columns [29]. Ismail proposed a novel elastoplastic bracing system consisting of a deformable steel ring at its core and four surrounding steel arcs. In this bracing system, each arc is tangentially connected to the central ring, then to the adjacent arc, and ultimately directly or through a rigid arm to the corner of the frame. He examined the capability of this bracing system to control structural vibrations and other vibration-related responses through numerical investigations under natural and artificial dynamic excitations. These examinations revealed that this bracing system could effectively mitigate and control structural vibrations at a low cost. As a result, it can be considered a viable and cost-effective substitute for conventional bracing systems [30]. Fanaie and Shirpour introduced a novel solution, the quarter-elliptic-braced steel moment frame (QEB-MF), to address the shortcomings of previous CBF systems and the lack of connection between bracing members and frame members (beams and columns). An exact analytical formulation was presented, employing Castigliano's theorem and concepts of strain energy to compute the QEB-MF systems' lateral stiffness. This system's seismic performance was also evaluated and compared to moment-resisting frames under near-field and far-field ground motion records. The assessment of the findings has shown that incorporating this brace into the moment frame system improves its seismic performance [31].

Conventional building structures are loaded per regulations and codes, then undergo analysis and design. These structures generally demonstrate non-linear behavior during an earthquake and absorb substantial seismic energy by tolerating non-elastic deformations. Therefore, they can be designed to withstand seismic forces significantly lower than the required force in linear design. As a result, in order to facilitate and reduce computational costs, codes allow engineers to analyze and design building structures within the linear range by considering factors for applying non-linear effects. In this method, known as the equivalent lateral forces (ELF), the seismic performance factors (SPFs) that consider non-linear effects encompass the response modification factor (R), the deflection amplification factor (C_d), and the over-strength factor (Ω) [32–35]. The FEMA P695 methodology has been developed to provide a rational and standardized assessment of the seismic performance of building systems at the collapse level, along with its associated performance parameters [36]. In this approach, aimed at evaluating the seismic performance of structures, based on the flowchart

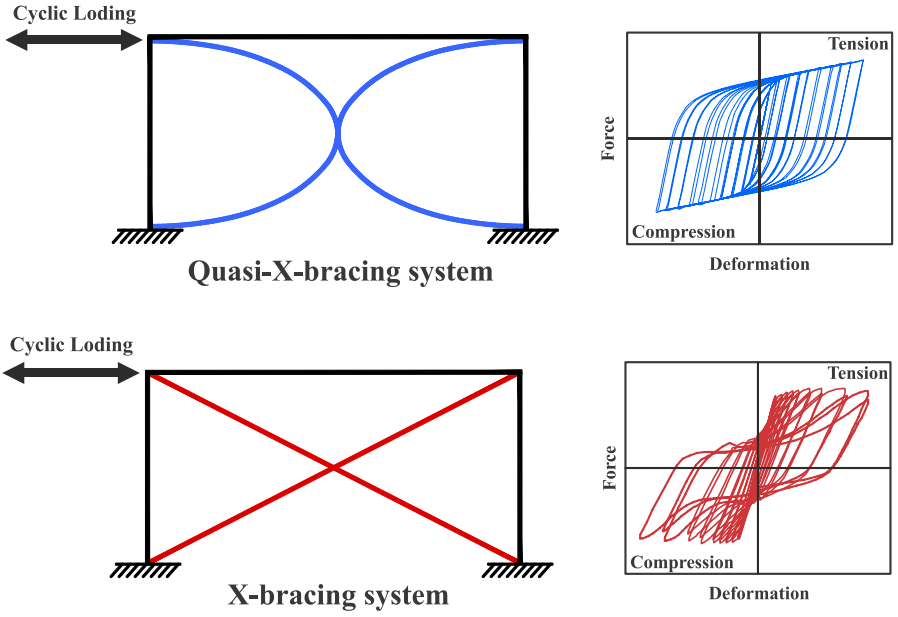

Fig. 2. Schematic diagram for the comparison of two quasi-X and X-bracing systems.

Table 1
Summary of QXB-MF and QIXB-MF performance groups.

PG NO.	Archetype ID		Design load level		Period domain	Number of stories
	Quasi-X-braced steel moment frame	Quasi inverse-X-braced steel moment frame	Gravity	Seismic		
PG-1	QXB-MF-2H	QIXB-MF-2H	Residential ($I_e = 1$)	SDC C_{max}	Short	2
PG-2	QXB-MF-4H	QIXB-MF-4H			Long	4
	QXB-MF-6H	QIXB-MF-6H				6
	QXB-MF-8H	QIXB-MF-8H				8
PG-3	QXB-MF-2L	QIXB-MF-2L		SDC C_{min}	Short	2
PG-4	QXB-MF-4L	QIXB-MF-4L			Long	4
	QXB-MF-6L	QIXB-MF-6L				6
	QXB-MF-8L	QIXB-MF-8L				8

shown in Fig. 1, the studied system's archetypes are first designed and developed by assuming structural information. Then, non-linear models are developed by considering stiffness and strength degradation for all members and are subjected to non-linear analyses. Finally, to validate the initial assumptions, the obtained values are compared to the acceptable values provided in the FEMA P695 guideline, and SPF factors are determined based on the total collapse uncertainty. This method uses probabilistic analyses and fragility curves derived from various earthquakes. Developing this method for new structural systems can enable the appropriate performance of structures against earthquakes and provide a new horizon for improving seismic design computations [37–39].

This paper aims to ascertain the seismic performance factors (SPFs) of two innovative bracing systems, called the quasi-X-braced steel moment frame (QXB-MF) and the quasi inverse-X-braced steel moment frame (QIXB-MF), as per the FEMA P695 methodology. These two systems comprise four quarter-elliptical bracing members to enhance ductility and energy dissipation. As shown in Fig. 2, implementing these bracing systems in buildings, as opposed to conventional CBFs (X-bracing systems), reduces the risk of establishing the first soft-story and overall building instability owing to hardening at large deformations. The quasi-X-bracing systems can be an appropriate alternative to BRBs due to their sustainable cyclic behavior and energy dissipation without stiffness and strength deterioration. In addition, the bracing members in these systems are not connected to the frame members (columns and beams), providing them with an advantage over circular and elliptical bracing systems.

In this study, eight three-dimensional 2-, 4-, 6-, and 8-story archetypes are designed for each of the bracing systems in the seismic design categories (SDC) C_{min} and C_{max} based on presumed SPFs. Each structural archetype's non-linear model is constructed in the OpenSees software, considering stiffness and strength degradation. At first, non-linear static (pushover) analysis is performed to validate the constructed non-linear models and compute each archetype's period-based ductility (μ_T) and over-strength factor (Ω). Next, incremental dynamic analysis (IDA) is conducted using 44 far-field ground motion (FFGM) records to estimate the collapse capacity of archetypes and calculate the adjusted collapse margin ratio (ACMR). The accuracy of the preliminary SPFs has been assessed by comparing the extracted ACMRs from the IDA curves with the acceptable values specified in FEMA P695. The results of this study indicate that the assumed initial R factor $(R = 5)$ for both quasi-X bracing systems can fulfill the desired performance and be employed as their R factor in design. In addition, this study has yielded values of 5 for the deflection amplification factor (C_d) and 3 for the over-strength factor (Ω).

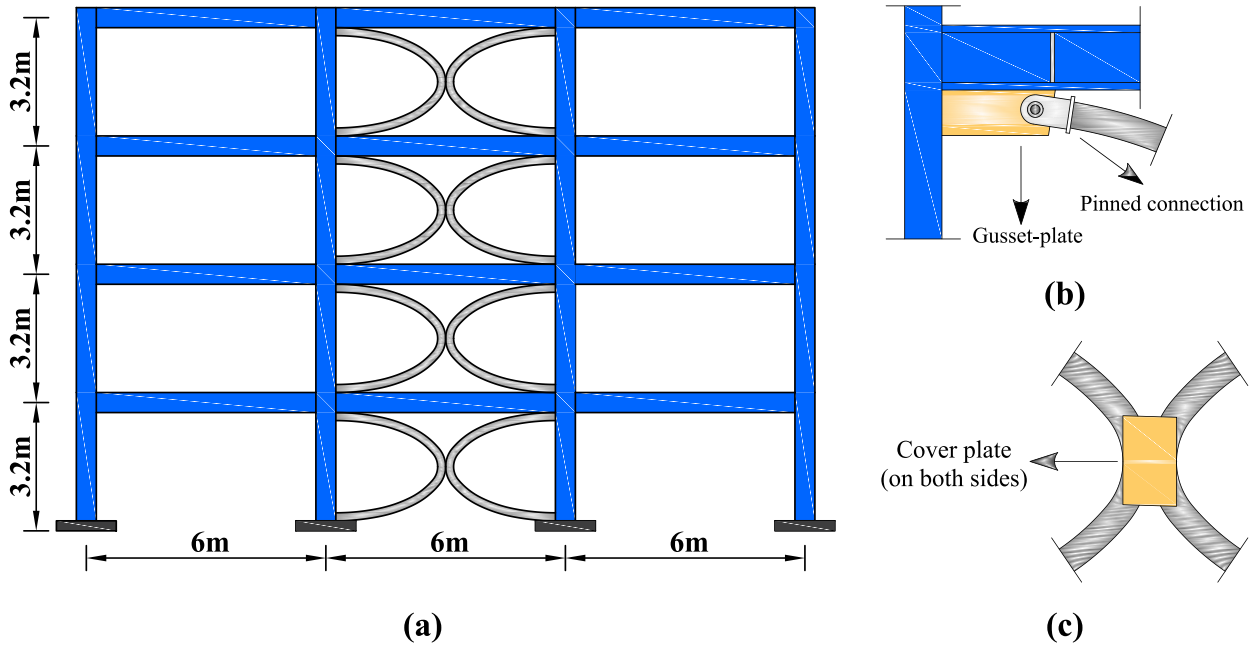

Fig. 3. Quasi-X-braced steel moment frame (QXB-MF); (a) Elevation view, (b) Corner-connection details, (c) Mid-connection details.

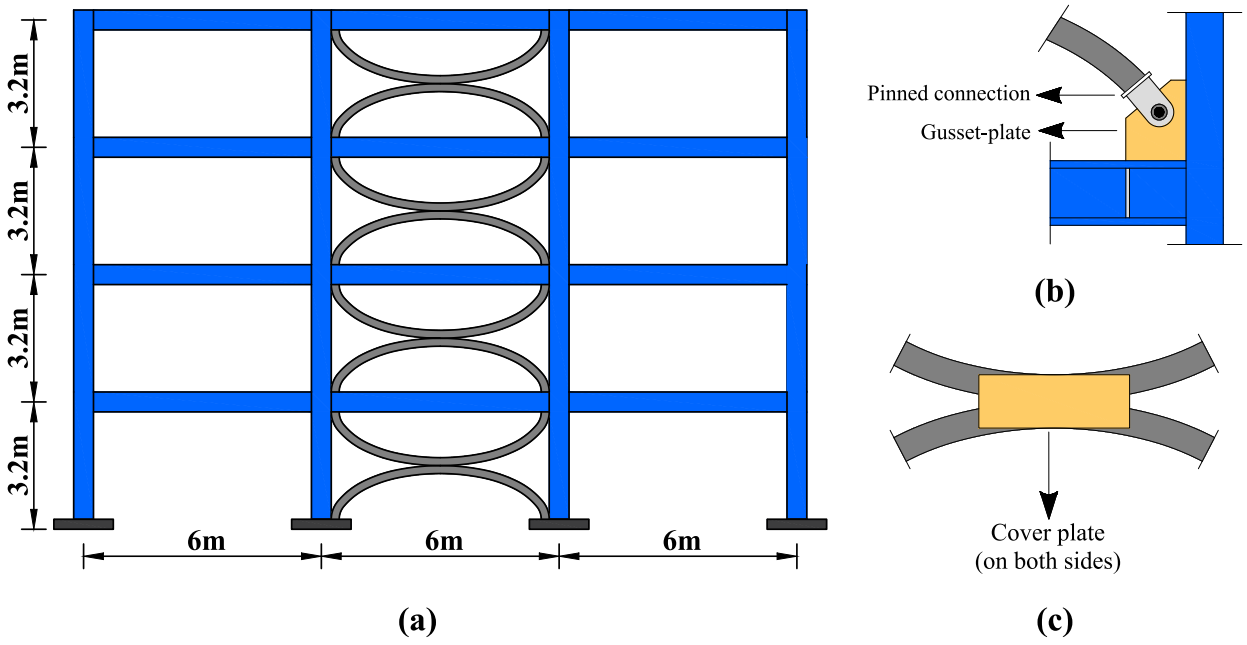

Fig. 4. Quasi inverse-X -braced steel moment frame (QIXB-MF); (a) Elevation view, (b) Corner-connection details, (c) Mid-connection details.

Table 2
Designated gravitational loads for designing archetypes.

	Dead (kN/m^2)	Live (kN/m^2)	Wall (kN/m^2)	Partition (kN/m^2)
Roof loads	4.80	1.50	1.76	0.00
Floor loads	4.30	2.00	1.76	0.50

2. Designing and developing structural archetypes

The first step in ensuring comprehensive coverage of the structural system's design space, as per the FEMA P695 procedure [36], is the careful choice of representative archetypes that appropriately account for all factors involving the arrangement and placement of the bracing system, the number of stories, and the intensity of gravitational loads. In this study, eight three-dimensional archetypes, ranging from 2 to 8 stories, were specifically considered for each bracing system in the seismic design categories (SDC) C_{min} and C_{max}. The archetypes were categorized into four performance groups based on their fundamental periods and SDCs. Table 1 presents the defined performance groups for the QXB-MF and QIXB-MF systems.

All desired structural system archetypes have a regular and symmetrical plan with three 6-m bays in each perpendicular direction. The archetypes are designed for residential purposes and are assigned an intermediate seismic importance factor ($I_e = 1$). Fig. 3 illustrates the QXB-MF bracing system and its connections, whereas Fig. 4 depicts the QIXB-MF bracing system and its connections.

Based on Figs. 3a and 4a, the perimeter frames in the archetypes are equipped with quasi-X-braces positioned within the frames' mid-bays, and the stories' height has been regarded as 3.2 *m*. In these bracing systems, as indicated in Figs. 3b and 4b, the beams are rigidly connected to the columns, and bracing members are connected to the gusset plates through pinned connections. Moreover, according to Figs. 3c and 4c, cover plates have been employed to ensure the integrative functioning of

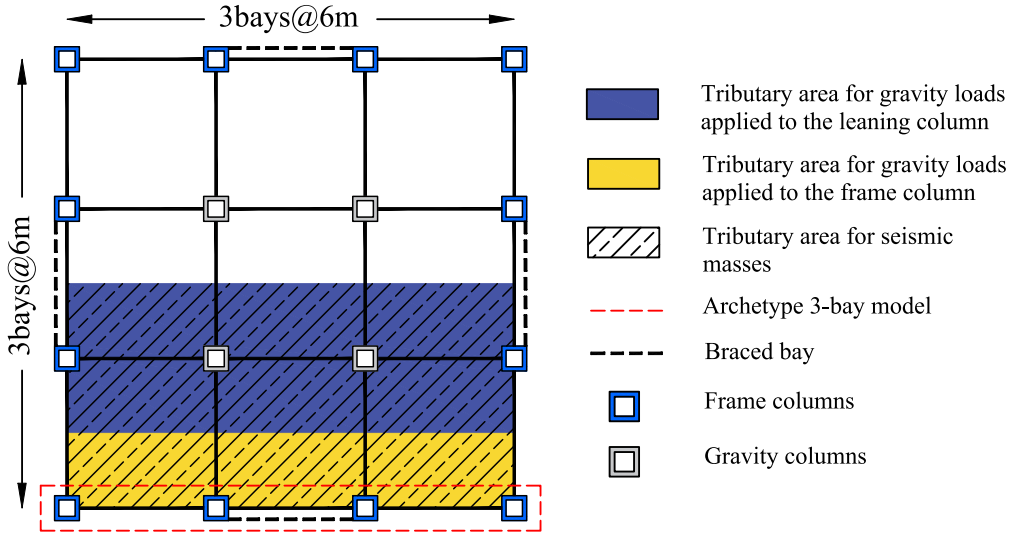

Fig. 5. Plan view of QXB-MF and QIXB-MF archetypes.

Table 3
The designed cross-sections for QXB-MF system archetypes.

PG NO.	Archetype ID	Story NO.	Column		Beam	Brace
			Exterior	Interior		
PG-1	QXB-MF-2H	1	BOX 200 × 10	BOX 200 × 10	IPE 300	BOX 100 × 10
		2	BOX 200 × 10	BOX 150 × 10	IPE 300	BOX 100 × 10
PG-2	QXB-MF-4H	1	BOX 300 × 10	BOX 300 × 10	IPE 360	BOX 100 × 10
		2	BOX 250 × 10	BOX 250 × 10	IPE 360	BOX 100 × 10
		3	BOX 250 × 10	BOX 250 × 10	IPE 330	BOX 100 × 10
		4	BOX 200 × 10	BOX 200 × 10	IPE 300	BOX 100 × 10
	QXB-MF-6H	1	BOX 300 × 15	BOX 300 × 15	IPE 400	BOX 120 × 12
		2	BOX 300 × 10	BOX 300 × 10	IPE 400	BOX 120 × 12
		3	BOX 250 × 10	BOX 250 × 10	IPE 400	BOX 120 × 12
		4	BOX 250 × 10	BOX 250 × 10	IPE 360	BOX 100 × 10
		5	BOX 250 × 10	BOX 200 × 10	IPE 330	BOX 100 × 10
		6	BOX 200 × 10	BOX 200 × 10	IPE 300	BOX 100 × 10
	QXB-MF-8H	1	BOX 300 × 15	BOX 300 × 15	IPE 450	BOX 120 × 12
		2	BOX 300 × 15	BOX 300 × 15	IPE 450	BOX 120 × 12
		3	BOX 300 × 10	BOX 300 × 15	IPE 450	BOX 120 × 12
		4	BOX 250 × 10	BOX 300 × 10	IPE 450	BOX 120 × 12
		5	BOX 250 × 10	BOX 300 × 10	IPE 400	BOX 100 × 10
		6	BOX 250 × 10	BOX 250 × 10	IPE 360	BOX 100 × 10
		7	BOX 200 × 10	BOX 200 × 10	IPE 360	BOX 100 × 10
		8	BOX 200 × 10	BOX 200 × 10	IPE 270	BOX 100 × 10
PG-3	QXB-MF-2L	1	BOX 200 × 10	BOX 200 × 10	IPE 300	BOX 100 × 10
		2	BOX 200 × 10	BOX 150 × 10	IPE 270	BOX 100 × 10
	QXB-MF-4L	1	BOX 250 × 10	BOX 250 × 10	IPE 330	BOX 100 × 10
		2	BOX 250 × 10	BOX 200 × 10	IPE 330	BOX 100 × 10
		3	BOX 200 × 10	BOX 200 × 10	IPE 300	BOX 100 × 10
		4	BOX 200 × 10	BOX 200 × 10	IPE 270	BOX 100 × 10
PG-4	QXB-MF-6L	1	BOX 300 × 10	BOX 300 × 10	IPE 360	BOX 100 × 10
		2	BOX 250 × 10	BOX 300 × 10	IPE 360	BOX 100 × 10
		3	BOX 250 × 10	BOX 250 × 10	IPE 360	BOX 100 × 10
		4	BOX 200 × 10	BOX 200 × 10	IPE 330	BOX 100 × 10
		5	BOX 200 × 10	BOX 200 × 10	IPE 300	BOX 100 × 10
		6	BOX 200 × 10	BOX 200 × 10	IPE 270	BOX 100 × 10
	QXB-MF-8L	1	BOX 300 × 10	BOX 300 × 15	IPE 360	BOX 120 × 12
		2	BOX 300 × 10	BOX 300 × 10	IPE 360	BOX 120 × 12
		3	BOX 250 × 10	BOX 300 × 10	IPE 360	BOX 100 × 10
		4	BOX 250 × 10	BOX 250 × 10	IPE 360	BOX 100 × 10
		5	BOX 250 × 10	BOX 250 × 10	IPE 360	BOX 100 × 10
		6	BOX 200 × 10	BOX 200 × 10	IPE 330	BOX 100 × 10
		7	BOX 200 × 10	BOX 200 × 10	IPE 330	BOX 100 × 10
		8	BOX 200 × 10	BOX 150 × 10	IPE 270	BOX 100 × 10

bracing members at the mid-connections [40]. In this research, IPE cross-sections were utilized for beams and BOX cross-sections for columns and bracing members. Also, S235JR steel grade was used for all members complying with the EN1993-1-1 standard [41] with mechanical properties $F_y = 235\ MPa$, $F_u = 360\ MPa$, and $E = 210000\ MPa$. The gravity load-resisting system for all archetypes' floors was considered the composite steel deck (assuming a rigid floor diaphragm). The design basis gravity loads for all archetypes were determined per the live load and dead load standard values specified in the ASCE/SEI 7–22 standard [42]. Table 2 illustrates the assigned values for gravitational dead and live loads.

All archetypes were subjected to seismic loading conforming to ASCE/SEI 7–22 [42], considering the R factor of 6.5 as well as the effects of P-Delta and the vertical earthquake. Given the regularity of the archetypes in both plan and elevation, the EFL analysis method was employed for their design in the ETABS software. The archetypes have been designed in accordance with the ANSI/AISC 360–16 standard [43] and the ANSI/AISC 341–16 seismic provision [44]. Additionally, the control of stories' drift and structural stability after design was conducted per the ASCE/SEI 7–22 standard [42].

3. Non-linear modeling

The OpenSees software was employed to model and analyze the studied non-linear archetypes, as it adheres to the appointed circumstances outlined in the FEMA P695 guidelines [36,45]. Among these circumstances, it is notable to mention the capability of conducting non-linear static analysis and non-linear dynamic analysis of time history, as well as considering stiffness and strength degradation. Two-dimensional models are utilized for non-linear analyses due to the regularity in the investigated archetypes' elevation and plan, which reduces the computational cost. For this reason, a side frame in the x-direction, as shown in Fig. 5, was chosen for each archetype and modeled in the OpenSees software. Tables 3 and 4 present the designed cross-sections for two-dimensional QXB-MF and QIXB-MF frames, respectively.

In order to avoid errors in seismic force calculation resulting from ground motion records and dynamic analysis during structural vibration, it is crucial to accurately convert the structural mass from a three-dimensional model to a two-dimensional model. Due to the structural symmetry in the plan, the two-dimensional frames supply half of the lateral stiffness of their corresponding three-dimensional structures in the x-direction. Therefore, to ensure precise modeling, 50% of the three-dimensional structures' total mass, comprising dead loads and a

Table 4
The designed cross-sections for QIXB-MF system archetypes.

PG NO.	Archetype ID	Story NO.	Column		Beam	Brace
			Exterior	Interior		
PG-1	QIXB-MF-2H	1	BOX 200 × 10	BOX 200 × 10	IPE 300	BOX 100 × 10
		2	BOX 200 × 10	BOX 150 × 10	IPE 300	BOX 100 × 10
PG-2	QIXB-MF-4H	1	BOX 300 × 10	BOX 300 × 10	IPE 360	BOX 100 × 10
		2	BOX 250 × 10	BOX 250 × 10	IPE 360	BOX 100 × 10
		3	BOX 250 × 10	BOX 200 × 10	IPE 330	BOX 100 × 10
		4	BOX 250 × 10	BOX 200 × 10	IPE 300	BOX 100 × 10
	QIXB-MF-6H	1	BOX 300 × 15	BOX 300 × 15	IPE 360	BOX 120 × 12
		2	BOX 300 × 10	BOX 300 × 10	IPE 360	BOX 120 × 12
		3	BOX 250 × 10	BOX 250 × 10	IPE 360	BOX 120 × 12
		4	BOX 250 × 10	BOX 250 × 10	IPE 360	BOX 100 × 10
		5	BOX 250 × 10	BOX 200 × 10	IPE 330	BOX 100 × 10
		6	BOX 200 × 10	BOX 200 × 10	IPE 300	BOX 100 × 10
	QIXB-MF-8H	1	BOX 300 × 15	BOX 300 × 15	IPE 400	BOX 120 × 12
		2	BOX 300 × 15	BOX 300 × 15	IPE 400	BOX 120 × 12
		3	BOX 300 × 10	BOX 300 × 15	IPE 400	BOX 120 × 12
		4	BOX 300 × 10	BOX 300 × 10	IPE 400	BOX 120 × 12
		5	BOX 250 × 10	BOX 300 × 10	IPE 360	BOX 100 × 10
		6	BOX 250 × 10	BOX 250 × 10	IPE 360	BOX 100 × 10
		7	BOX 250 × 10	BOX 200 × 10	IPE 330	BOX 100 × 10
		8	BOX 200 × 10	BOX 200 × 10	IPE 300	BOX 100 × 10
PG-3	QIXB-MF-2L	1	BOX 200 × 10	BOX 200 × 10	IPE 300	BOX 100 × 10
		2	BOX 200 × 10	BOX 150 × 10	IPE 270	BOX 100 × 10
PG-4	QIXB-MF-4L	1	BOX 250 × 10	BOX 250 × 10	IPE 330	BOX 100 × 10
		2	BOX 250 × 10	BOX 200 × 10	IPE 330	BOX 100 × 10
		3	BOX 200 × 10	BOX 200 × 10	IPE 300	BOX 100 × 10
		4	BOX 200 × 10	BOX 150 × 10	IPE 270	BOX 100 × 10
	QIXB-MF-6L	1	BOX 300 × 10	BOX 300 × 10	IPE 360	BOX 100 × 10
		2	BOX 250 × 10	BOX 250 × 10	IPE 360	BOX 100 × 10
		3	BOX 250 × 10	BOX 250 × 10	IPE 330	BOX 100 × 10
		4	BOX 250 × 10	BOX 200 × 10	IPE 330	BOX 100 × 10
		5	BOX 200 × 10	BOX 200 × 10	IPE 300	BOX 100 × 10
		6	BOX 200 × 10	BOX 150 × 10	IPE 270	BOX 100 × 10
	QIXB-MF-8L	1	BOX 300 × 15	BOX 300 × 15	IPE 360	BOX 120 × 12
		2	BOX 300 × 10	BOX 300 × 15	IPE 360	BOX 120 × 12
		3	BOX 300 × 10	BOX 300 × 10	IPE 360	BOX 100 × 10
		4	BOX 250 × 10	BOX 250 × 10	IPE 360	BOX 100 × 10
		5	BOX 250 × 10	BOX 250 × 10	IPE 330	BOX 100 × 10
		6	BOX 200 × 10	BOX 200 × 10	IPE 330	BOX 100 × 10
		7	BOX 200 × 10	BOX 200 × 10	IPE 300	BOX 100 × 10
		8	BOX 200 × 10	BOX 150 × 10	IPE 270	BOX 100 × 10

percentage of live loads, was extracted from the ETABS software and applied as a concentrated mass to column element end nodes at each story. Moreover, the leaning columns bear the gravitational loads arising from the elimination of the middle frames.

Fig. 6 demonstrates the complete non-linear modeling of the QXB-MF and QIXB-MF archetypes, encompassing the deterioration model, the appointed elements for members, the panel zone, and the leaning column.

According to this figure, the concentrated-plasticity modeling approach was utilized to consider the members' softening and degradation in the examined archetypes. This approach was selected due to the lack of two low-cycle fatigue parameters for elliptical braces [46]. Accordingly, plastic hinges were placed at the ends of the columns and beams, while their middle elements were treated as elastic. A combination of twelve elastic elements and five plastic hinges was employed to enhance the precision of modeling the quarter-elliptical bracing members. The structure-soil interaction effects were ignored in this study, and structural connections have been modeled as fixed supports.

The modified Ibarra-Medina-Krawinkler (ModIMK) deterioration model combining a bilinear hysteretic response (Bilin Material) was utilized to determine all members' moment-rotation behavior [47–49]. Consideration of stiffness and strength degradation is a key feature of this model, and this degradation is reliant on the loading history. Fig. 7a depicts the ModIMK model, which encompasses various effective parameters. These parameters, as indicated in the figure, include effective elastic stiffness (K_e), capping strength and associate rotation for monotonic loading $(M_c \text{ and } \theta_c)$, effective yield strength and rotation $(M_y \text{ and } \theta_y)$, residual strength (M_r), pre-capping rotation capacity for monotonic loading (θ_p), post-capping rotation capacity (θ_{pc}), cyclic deterioration parameter (κ), and ultimate rotation capacity (θ_u). Between 2012 and 2019, Lignous et al. undertook a comprehensive study examining experimental samples' behavior. They used statistical regression analysis to evaluate the data and derive relationships for the parameters mentioned [47–49]. Due to the necessity of performing both non-linear dynamic and non-linear static analyses for determining the SPFs, the values of these parameters vary for each analysis according to the NIST 2017b [50]. This guideline recommends that the equations related to the first cycle envelope curve be utilized for non-linear static analysis, as they consider the degradation and reduction in strength parameters. Also, the equations associated with the monotonic backbone curve are used to estimate the parameters for the non-linear dynamic analysis. Based on the ASCE/SEI 7–22 standard's recommendation, the Rayleigh damping model with a damping ratio of 2.5% has been employed for all archetypes, considering the period of the primary two modes [42]. In order to simulate the rigid floor diaphragm

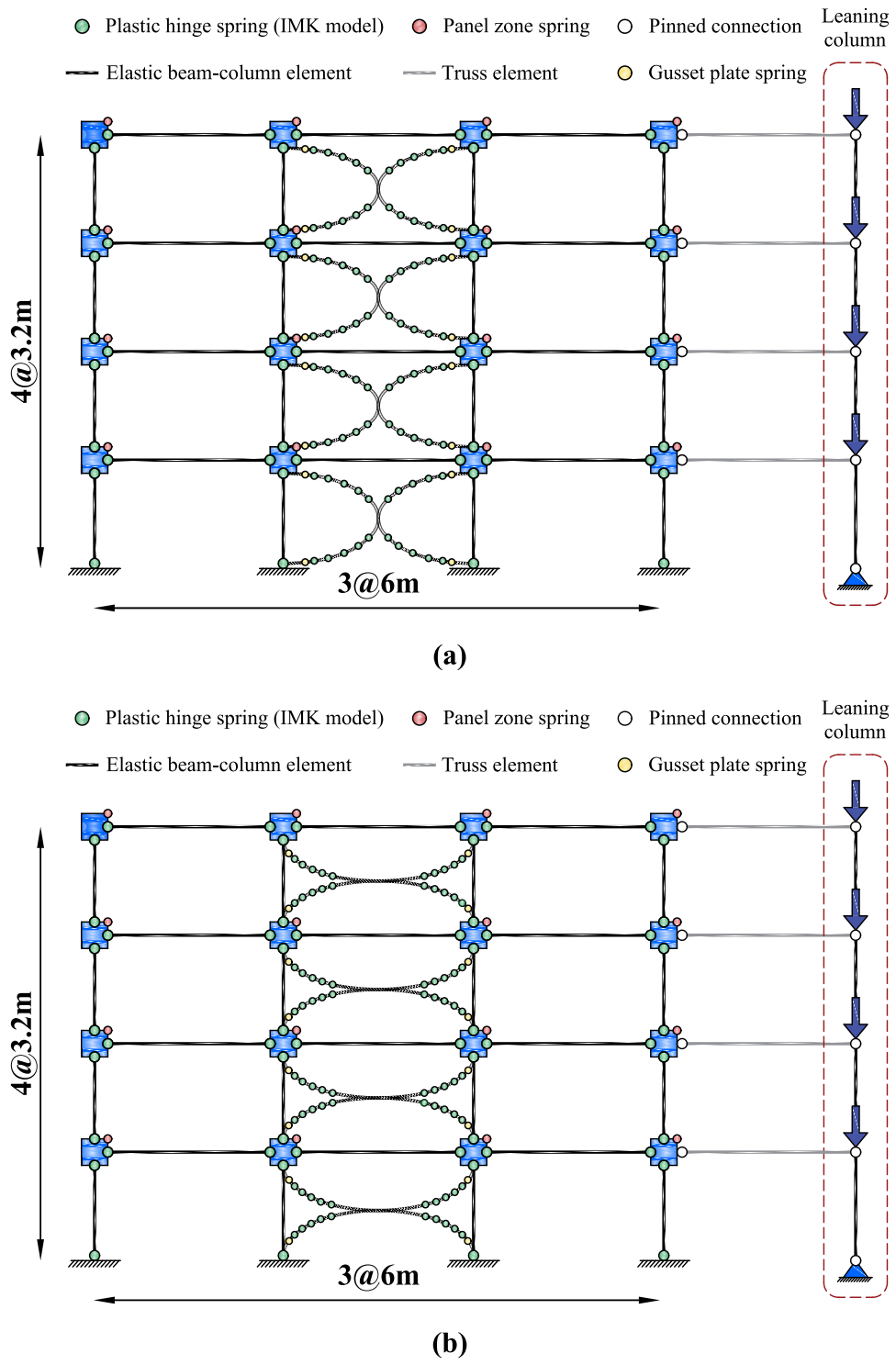

Fig. 6. Non-linear modeling of archetypes; (a) QXB-MF system, (b) QIXB-MF system.

in OpenSees software, the nodes at each story level were constrained using the equalDOF command [45]. The panel zone is where beams and columns are connected, and this region is subjected to axial, shear, and bending forces resulting from the beams and columns. The panel zone modeling not only reduces the beam and column spans' free length and enhances structural stiffness but also considers the deformation owing to the elastic and plastic behavior of the panel zone in the structure's dynamic behavior. The predominant factor affecting the panel zone's response is usually shear forces. In this study, the panel zone was modeled using the Gupta and Krawinkler method to achieve complete and precise modeling [51]. This method considers the panel zone with eight rigid elements and a rotational spring in a rectangular configuration, as depicted in Fig. 7b. The rotational spring simulates the shear force-deformation behavior in the panel zone using hysteretic materials with trilinear behavior. The curve of this material depends on the steel materials' properties, the geometric characteristics of the beams and columns, and the yield strength and strain hardening coefficients.

During modeling a two-dimensional frame in the OpenSees software, the leaning column is employed to consider the effects of other parallel frames with the examined frame in three-dimensional space and the P-

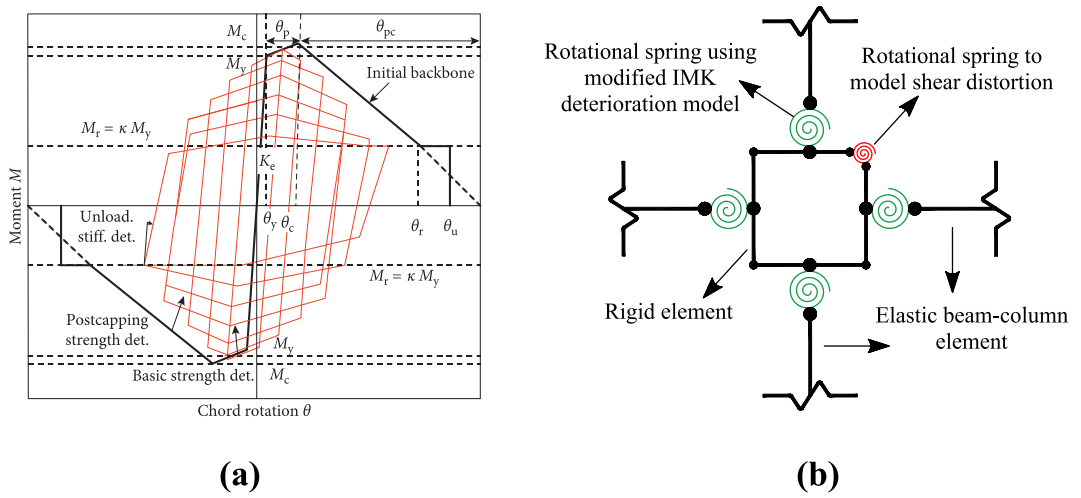

Fig. 7. OpenSees non-linear modeling; (a) ModIMK deterioration model, (b) Components of Krawinkler's panel zone model.

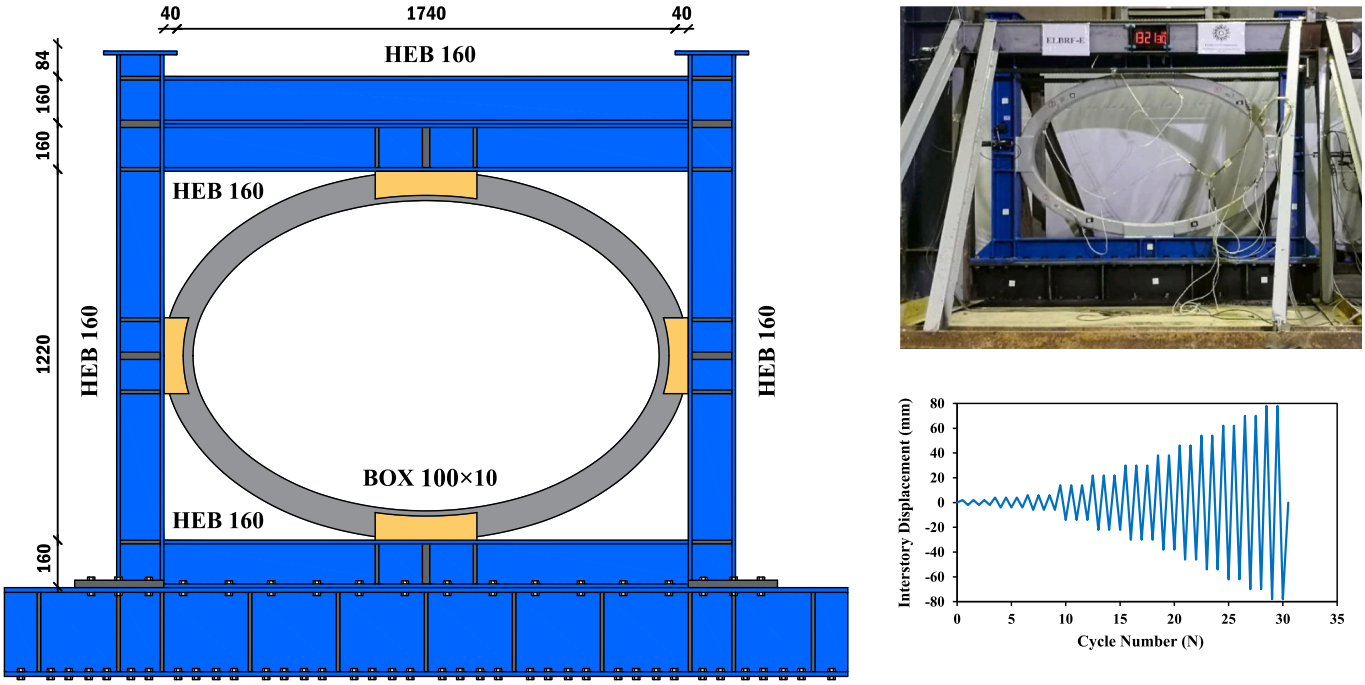

Fig. 8. Experimental test details of ELBRF system [28].

Table 5
Mechanical properties of steel materials from the tensile coupon tests [28].

Sections	$F_y[N/mm^2]$	$F_u[N/mm^2]$	$E[N/mm^2]$	Yield strain	Hardening strain	Ultimate strain
HEB 160	355	512	203,200	0.17%	1.86%	25%
BOX 100 × 10	360	551	205,600	0.18%	3.28%	20%

Delta effects. To this end, an extra bay was added to the frame, and the extracted loads from the middle frames were applied to this bay's column. This bay's columns were connected to the master frame via the pinned connections. In order to prevent the entrance of additional moments into the master frame, rigid elements were employed for the columns, while truss elements were utilized for the beams. Additionally, the leaning columns were connected by rotational springs with negligible stiffness to eliminate moment absorption [50].

4. Validation and verification of non-linear modeling

In this study, the accuracy of the non-linear modeling was validated utilizing the results obtained from experimental studies performed by Jouneghani et al. on an elliptical braced resisting frame (ELBRF) [28]. They constructed a single-span and single-story elliptical bracing frame and subjected it to quasi-static loading in the laboratory using hydraulic jacks. In this model, all the connections between beams and columns, as well as braces and frame members, were rigidly implemented. The frame height and width have been specified to be 1.5 *m* and 2 *m*, respectively,

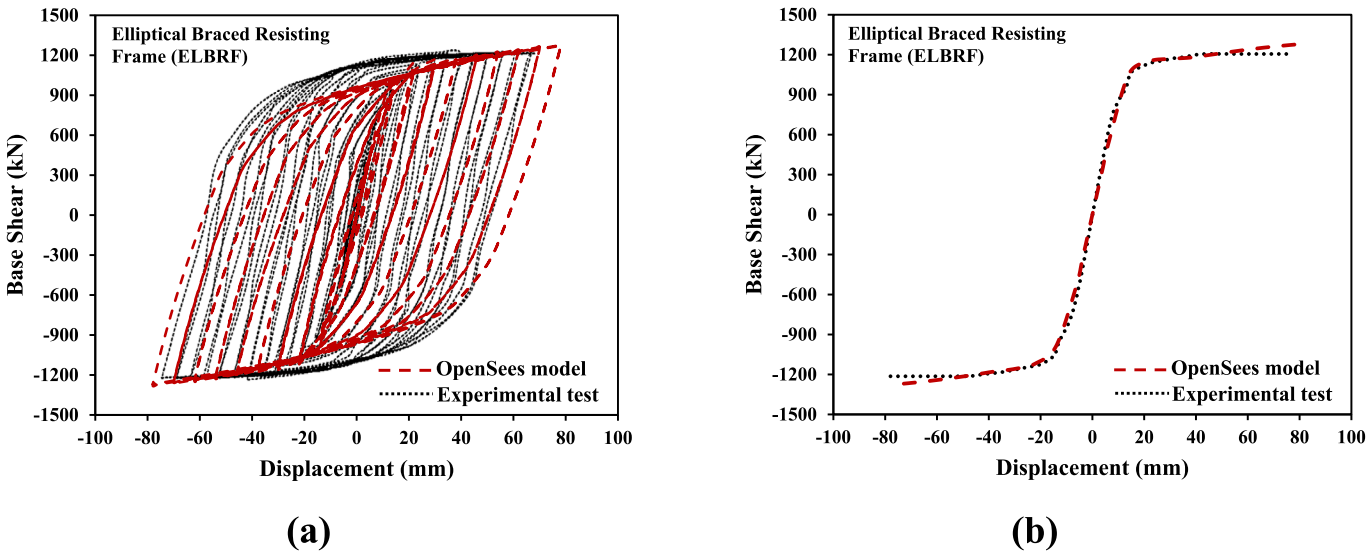

Fig. 9. Comparison of the numerical model and experimental test of the ELBRF system; (a) Hysteresis curves, (b) Backbone curves.

according to Fig. 8. The beams and columns were constructed using HEB cross-sections, whereas the bracing member was executed utilizing a BOX cross-section. Also, the bracing frame was subjected to quasi-static loading using the ATC-24 loading protocol [52]. The mechanical properties of the steel materials used for the cross-sections, obtained through tensile coupon testing, are presented in Table 5.

The desired bracing frame was modeled in OpenSees software under cyclic loading in order to validate the accuracy of non-linear modeling. To accomplish this, the concentrated plasticity method with the Mod-IMK deterioration model and Krawinkler's panel zone model was utilized for the non-linear modeling of the bracing frame [47–49,51]. The hysteresis curve obtained from the numerical analysis results was compared with the experimental hysteresis curve. The hysteresis and backbone curves for the ELBRF system are presented in Figs. 9a and b, respectively.

The comparison of the curves demonstrates appropriate conformity between the numerical and experimental results. The tiny observed discrepancy in the hysteresis curves and energy absorption of the bracing frame is due to the absence of modeling of details, such as stiffeners, in the OpenSees software.

5. Non-linear analysis

5.1. Non-linear static (pushover) analysis

Based on the steps provided in FEMA P695 [36], determining the values of the period-based ductility (μ_T) and the over-strength (Ω) factors for all archetypes is necessary to assess the seismic performance of quasi-X bracing systems. The best approach for attaining this goal is to use non-linear static (pushover) analysis. In order to carry out a pushover analysis, it is imperative to identify and apply both lateral static loads and gravity loads to the structure. For considering the second-order effect (P-Delta) in pushover analysis, according to FEMA P695, the frames are subjected to gravitational loads using the load combination defined in Eq. (1):

$$1.05D + 0.25L \tag{1}$$

where D and L denote the nominal values of dead and live loads, respectively. The coefficients provided in this equation represent the anticipated values of loads, assuming a normal probability distribution. Also, the seismic-induced lateral forces are distributed along the structure's height, regarding the structure's first mode and the effective mass of each floor, as outlined in Eq. (2):

$$F_x \propto m_x \varphi_{1,x} \tag{2}$$

In the aforementioned equation, at each floor level (x), F_x, m_x, and $\varphi_{1,x}$ denote the lateral force distribution in height, the structure's mass, and the structure's first mode, respectively. Figs. 10 and 11 illustrate the pushover curves of the QXB-MF and QIXB-MF archetypes, respectively. In these figures, V, V_{max}, and W express the design base shear, the maximum base shear capacity in pushover analysis, and the structure's total weight, respectively. C_s represents the seismic response coefficient in ELF analysis, which is calculated for each archetype complying with ASCE/SEI 7–22 [42].

The Ω factor is computed using Eq. (3):

$$\Omega = \frac{V_{max}}{V} = \frac{V_{max}}{C_s W} \tag{3}$$

The ultimate displacement of the structure's roof, δ_u, is achieved at a specific point on the pushover curve, where the maximum base shear has been reduced by 20%. Additionally, the effective yield displacement of the structure's roof, $\delta_{y,eff}$, is computed through Eq. (4):

$$\delta_{y,eff} = C_0 \frac{V_{max}}{W} \left[\frac{g}{4\pi^2}\right] (max(T, T_1))^2 \tag{4}$$

where T, T_1, and g denote the structure's fundamental period gained via ASCE/SEI 7–22 standard relationships [42], the structure's fundamental vibration period acquired through the eigenvalue analysis, and gravitational acceleration, respectively. Furthermore, C_0 is the first-mode excitation coefficient at the structure's roof level, which is computed in compliance with the ASCE/SEI 41–06 standard [53] utilizing Eq. (5):

$$C_0 = \varphi_{1,r} \frac{\sum_{x=1}^{N} m_x \varphi_{1,x}}{\sum_{x=1}^{N} m_x {\varphi_{1,x}}^2} \tag{5}$$

where m_x, and $\varphi_{1,x}$ denote the structure's mass and the structure's first mode at each floor level (x). N represents the total number of floors, and $\varphi_{1,r}$ represents the structure's first mode at the roof level. The μ_T factor is computed using Eq. (6):

$$\mu_T = \frac{\delta_u}{\delta_{y,eff}} \tag{6}$$

Tables 6 and 7 present the outcomes gained from the pushover curves of the QXB-MF and QIXB-MF archetypes employing the mentioned equations, respectively. Based on these tables, in both SDCs, the maximum Ω factor has been observed for the 2-story quasi-X bracing

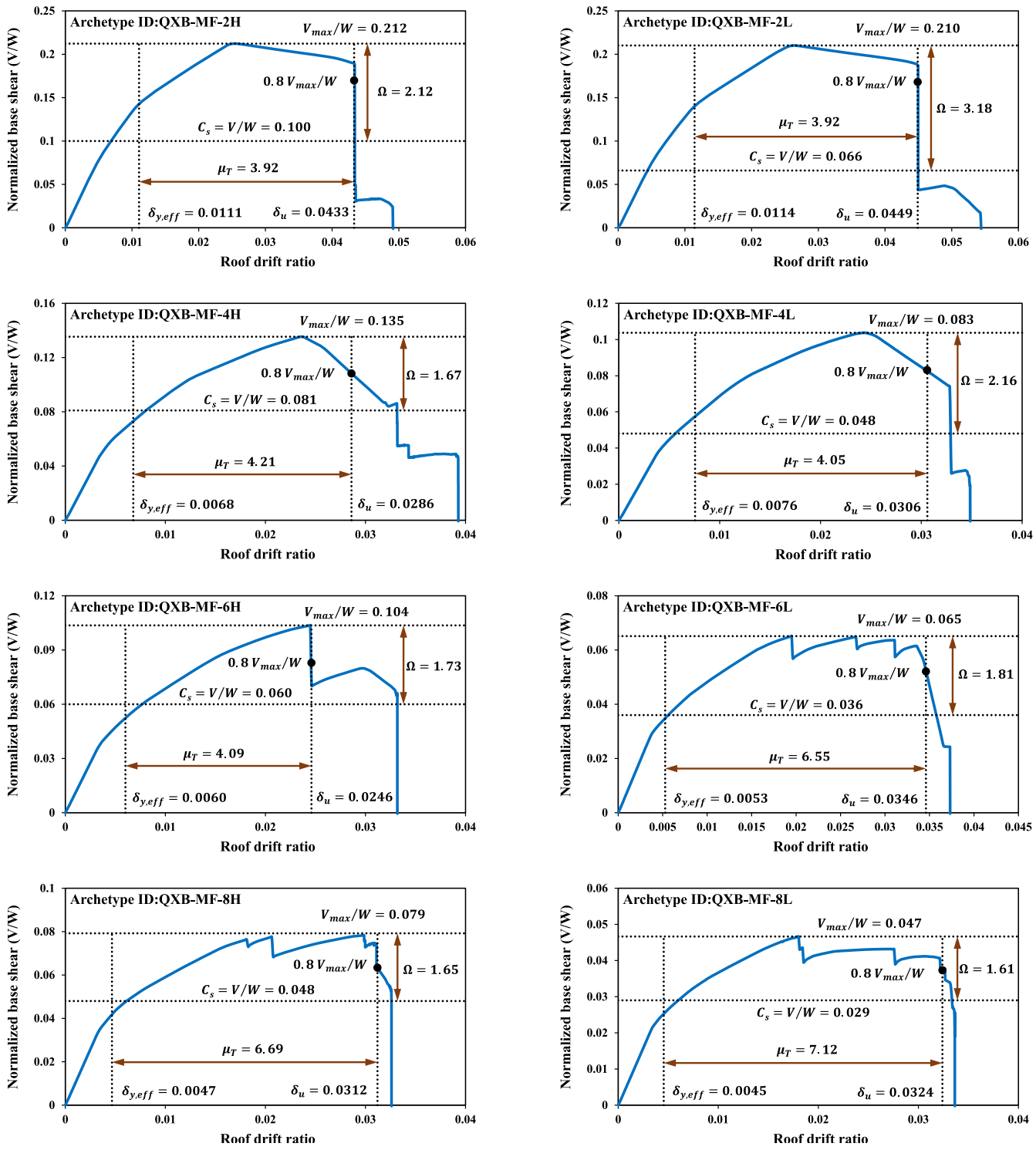

Fig. 10. Pushover curves of the QXB-MF archetypes.

archetypes, while the maximum μ_T factor has been observed for the 8-story quasi-X bracing archetypes.

5.2. Incremental dynamic analysis (IDA)

According to the procedures presented in FEMA P695 [37], in order to determine the SPFs of quasi-X bracing systems, the value of adjusted collapse margin ratio (ACMR) needs to be obtained for all archetypes utilizing incremental dynamic analysis (IDA). In the FEMA P695 methodology [37], the assessment of the seismic response of archetypes in non-linear dynamic analysis takes into account two sets of records: near-field ground motion (NFGM) and far-field ground motion (FFGM) records. The FFGM records comprise 22 pairs of horizontal records located 10 *km* or more from the fault rupture line, whereas the NFGM records comprise 28 pairs of horizontal records located less than 10 *km* from the fault rupture line. FEMA P695 employs FFGM records to evaluate the seismic performance of archetypes designed in SDC B, C, and D. On the other hand, NFGM records are utilized in particular studies to assess the seismic performance of archetypes designed in SDC E [36–39]. In this study, only FFGM records have been utilized to assess the archetypes'

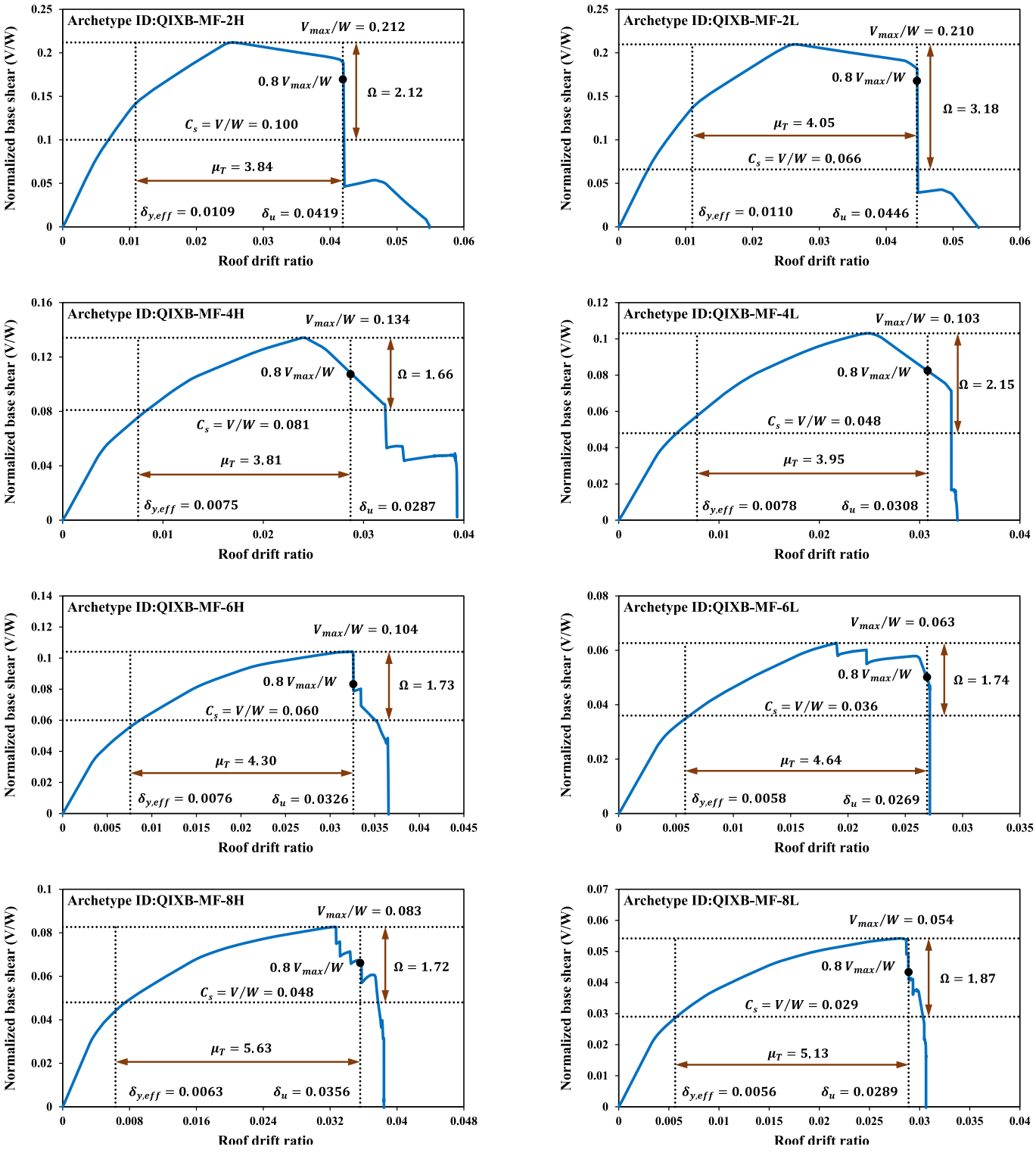

Fig. 11. Pushover curves of the QIXB-MF archetypes.

seismic performance. Table 8 presents utilized FFGM records, whose acceleration spectra and median response spectrum are depicted in Fig. 12.

The choice of appropriate parameters for intensity measure (IM) and damage measure (DM) is essential in IDA analysis. The meticulous selection of a well-suited IM reduces the dispersion in the structural responses when subjected to various earthquakes. Consequently, this facilitates more precise estimations of statistical indicators associated with these responses. According to the prevailing approach in various studies and recommendations stipulated by FEMA P695 [36], this parameter was considered equivalent to the first mode-5% damped spectral acceleration $S_a\,(T_1, 5\%)$. Likewise, the DM parameter was considered equivalent to the maximum inter-story drift ratio (MIDR) in this study. The collapse criteria specified by FEMA P695 were taken into account during the IDA analysis. These criteria comprised reducing the IDA curve's slope to 20% of the initial elastic slope, dynamic instability,

Table 6
Outcomes of modal and pushover analysis of QXB-MF system archetypes.

PG NO.	Archetype ID	$T(s)$	T_1/T	V_{max}/W	C_s	C_0	$\delta_{y,eff}(\%)$	$\delta_u(\%)$	μ_T	Ω	Ω_{ave}
PG-1	QXB-MF-2H	0.29	3.63	0.212	0.100	1.212	1.106	4.33	3.92	2.12	2.12
PG-2	QXB-MF-4H	0.49	2.86	0.135	0.081	1.317	0.679	2.86	4.21	1.67	1.68
	QXB-MF-6H	0.67	2.71	0.104	0.060	1.357	0.601	2.46	4.09	1.73	
	QXB-MF-8H	0.82	2.53	0.079	0.048	1.405	0.467	3.12	6.69	1.65	
PG-3	QXB-MF-2L	0.32	3.36	0.210	0.066	1.214	1.145	4.49	3.92	3.18	3.18
PG-4	QXB-MF-4L	0.54	3.14	0.104	0.048	1.304	0.756	3.06	4.05	2.16	1.86
	QXB-MF-6L	0.74	2.91	0.065	0.036	1.353	0.528	3.46	6.55	1.81	
	QXB-MF-8L	0.92	2.94	0.047	0.029	1.373	0.455	3.24	7.12	1.61	

Table 7
Outcomes of modal and pushover analysis of QIXB-MF system archetypes.

PG NO.	Archetype ID	$T(s)$	T_1/T	V_{max}/W	C_s	C_0	$\delta_{y,eff}(\%)$	$\delta_u(\%)$	μ_T	Ω	Ω_{ave}
PG-1	QIXB-MF-2H	0.29	3.61	0.212	0.100	1.212	1.091	4.19	3.84	2.12	2.12
PG-2	QIXB-MF-4H	0.49	3.03	0.134	0.081	1.309	0.753	2.87	3.81	1.66	1.70
	QIXB-MF-6H	0.67	3.06	0.104	0.060	1.342	0.758	3.26	4.30	1.73	
	QIXB-MF-8H	0.82	2.90	0.083	0.048	1.392	0.632	3.56	5.63	1.72	
PG-3	QIXB-MF-2L	0.32	3.30	0.210	0.066	1.214	1.100	4.46	4.05	3.18	3.18
PG-4	QIXB-MF-4L	0.54	3.19	0.103	0.048	1.311	0.781	3.08	3.95	2.15	1.92
	QIXB-MF-6L	0.74	3.13	0.063	0.036	1.332	0.579	2.69	4.64	1.74	
	QIXB-MF-8L	0.92	3.06	0.054	0.029	1.350	0.563	2.89	5.13	1.87	

Table 8
FEMA P695 far field ground motion record set.

ID No.	Event name	Year	Magnitude	Station	Site class (NEHRP)	PGA_{max} (g)	PGV_{max} (cm/s)
1	Northridge	1994	6.7	Beverly hills	D	0.52	63
2	Northridge	1994	6.7	Canyon country-WLC	D	0.48	45
3	Duzce, Turkey	1999	7.1	Bolu	D	0.82	62
4	Hector Mine	1999	7.1	Hector	C	0.34	42
5	Imperial valley	1979	6.5	El Centro array # 11	D	0.38	33
6	Imperial valley	1979	6.5	Delta	D	0.35	42
7	Kobe, Japan	1995	6.9	Nishi-Akashi	C	0.51	37
8	Kobe, Japan	1995	6.9	Shin-Osaka	D	0.24	38
9	Kocaeli, Turkey	1999	7.5	Duzce	D	0.36	59
10	Kocaeli, Turkey	1999	7.5	Arcelik	C	0.22	40
11	Landers	1992	7.3	Yermo Fire Station	D	0.24	52
12	Landers	1992	7.3	Coolwater	D	0.42	42
13	Loma Prieta	1989	6.9	Capitola	D	0.53	35
14	Loma Prieta	1989	6.9	Gilroy Array # 3	D	0.56	45
15	Manjil, Iran	1990	7.4	Abbar	C	0.51	54
16	Superstition Hills	1987	6.5	El Centro Imp. Co. Cent	D	0.36	46
17	Superstition Hills	1987	6.5	Poe Road	D	0.45	36
18	Cape Mendocino	1992	7.0	Rio dell overpass	D	0.55	44
19	Chi-Chi Taiwan	1999	7.6	CHY101	D	0.44	115
20	Chi-Chi Taiwan	1999	7.6	TCU045	C	0.51	39
21	San Fernando	1971	6.6	LA-Hollywood Stor FF	D	0.21	19
22	Friuli, Italy	1976	6.5	Tolmezzo	C	0.35	31

a substantial increase in inter-story drift, and non-simulated fractures. Pre-determining the necessary steps for gaining collapse in the IDA analysis is impractical, and the number of such analyses may be substantial due to the time-intensive nature of reaching the collapse threshold. In order to address this challenge, the advanced "hunt and fill" algorithm was utilized to minimize the number of steps needed to reach the collapse point [54]. In this algorithm, a small initial IM value is first chosen to ensure the structure remains linear. Afterward, the algorithm continues through three subsequent phases:

- In the "hunt" phase, the values of IM increase exponentially at each step until reaching the first IM after the structural collapse.
- In the "bracket" phase, to precisely specify the collapse IM, the interval between the obtained point and the point before collapse is divided into smaller intervals, and this process continues until the desired exactness is gained.
- In the "fill" phase, the intervals between the initially extracted points from the first phase are filled with new points. Actually, this phase enhances the accuracy of plotting the IDA curve by increasing the number of points within the elastic region.

One of the primary reasons for plotting IDA curves is to determine the value of the median collapse intensity $(\widehat{S}_{CT})$, which denotes the intensity level at which half of the records lead to structural collapse. After

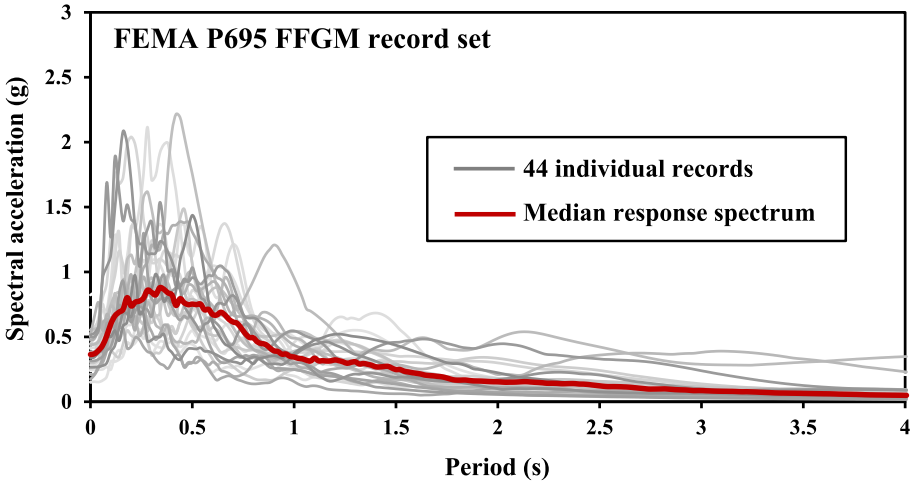

Fig. 12. Acceleration response spectra of the FEMA P695 FFGM records [36].

determining this value, it becomes possible to compute the structure's collapse margin ratio (CMR) value using Eq. (7) pursuant to FEMA P695 [36].

$$CMR = \frac{\widehat{S}_{CT}}{S_{MT}} \tag{7}$$

In this equation, S_{MT} denotes the maximum considered earthquake (MCE) ground motion intensity, which is acquired via the structure's fundamental period (T) for diverse SDCs as outlined in FEMA P695. Figs. 13 and 14 depict the IDA curves of the QXB-MF and QIXB-MF archetypes with 16%, 50%, and 84% fractile curves subjected to FFGM records, respectively. Examining the curves in these figures reveals that the $\widehat{S}_{CT}$ value has decreased as the number of archetypes' stories has increased in both SDC C_{max} and C_{min}. Baker and Cornell's research indicated that the CMR is impacted by both the seismic intensity and the frequency content of the records, particularly strong earthquakes [55]. The studies conducted by Haselton et al. reveal that the distinctive characteristic of these records is their spectral shape [56]. As a result, the structure exhibits less deterioration caused by these records than initially anticipated in the maximum period range, which undergoes a sharp decline in other periodic regions. For this reason, the CMR value increases by utilizing the spectral shape factor (SSF), and the adjusted collapse margin ratio (ACMR) is computed for each structure through Eq. (8). Following the tables presented in FEMA P695 [36], the SSF factor is specified for each archetype utilizing the μ_T factor and T (fundamental period).

$$ACMR = CMR \times SSF \tag{8}$$

The distribution of collapse capacity is affected by multiple sources of uncertainty. Based on FEMA P695 [36], the uncertainties that considerably impact the structures' seismic evaluation comprise modeling uncertainty (β_{MDL}), test data uncertainty (β_{TD}), design requirements uncertainty (β_{DR}), and record-to-record uncertainty (β_{RTR}). There are four possible values for each of the β_{MDL}, β_{TD}, and β_{DR} uncertainties: 0.1, 0.2, 0.35, or 0.5, depending on the corresponding quality level. Quality level A (superior) corresponds to a value of 0.1, quality level B (good) corresponds to 0.2, quality level C (fair) corresponds to 0.35, and quality level D (poor) corresponds to 0.5 in terms of quality rating.

In contrast, the β_{RTR} uncertainty is dependent on the value of the μ_T factor. According to FEMA P695, β_{RTR} is considered equal to 0.4 for structures with $\mu_T \geq 3$, while for structures with $\mu_T < 3$, it is computed using Eq. (9):

$$0.2 \leq \beta_{RTR} = 0.1 + 0.1\mu_T \leq 0.4 \tag{9}$$

Owing to the statistical independence of the aforementioned uncertainties, the standard deviation of the total collapse uncertainty (β_{TOT}) is computed utilizing Eq. (10):

$$\beta_{TOT} = \sqrt{{\beta_{MDL}}^2 + {\beta_{TD}}^2 + {\beta_{DR}}^2 + {\beta_{RTR}}^2} \tag{10}$$

In this study, quality level A (equal to 0.2) was considered for the β_{MDL}, β_{TD}, and β_{DR} uncertainties based on the archetypes' characteristics and their nonlinear modeling requirements. In light of Tables 6 and 7, μ_T is >3 for all QXB-MF and QIXB-MF archetypes. Therefore, β_{RTR} uncertainty is regarded as equal to 0.4 for all archetypes. Accordingly, β_{TOT} for all archetypes is calculated as equal to 0.529 using Eq. (10). The fragility curves depict the probability of structural collapse at various earthquake intensities, enabling the determination of the collapse probability per spectral acceleration level. Drawing these curves involves initially determining the spectral accelerations corresponding to collapse using IDA analysis for various records. Subsequently, a cumulative distribution function (CDF), such as the normal distribution function, is applied to this dataset to calculate the collapse probability for different spectral accelerations, facilitating the plotting of the fragility curve. Figs. 15 and 16 illustrate the fragility curves of the QXB-MF and QIXB-MF archetypes subjected to FFGM records, taking into account the uncertainties. These figures demonstrate two dashed fragility curves, where β_{RTR} and β_{TOT} are considered standard deviation parameters in the log-normal distribution. Besides, a solid fragility curve (shifted fragility curve) is depicted by multiplying the fragility curve with the standard deviation parameter β_{TOT} in SSF. As shown in Figs. 15 and 16, as the standard deviation amount increases, the slope of fragility curves decreases, and the collapse probability of S_{MT} increases.

6. Determination of seismic performance factors (SPFs)

6.1. *The response modification factor* (R)

Conforming to the FEMA P695 method [36], a structural system's seismic performance is deemed acceptable if both of the following conditions are fulfilled:

- The probability of collapse for each archetype under MCE earthquakes should be below 20%.
- The probability of collapse for each performance group under MCE earthquakes should be below 10%.

FEMA P695 indirectly assesses the expressed probable objectives by employing the acceptable value of ACMR. Accordingly, the presumed R factor is considered acceptable if the following two conditions are

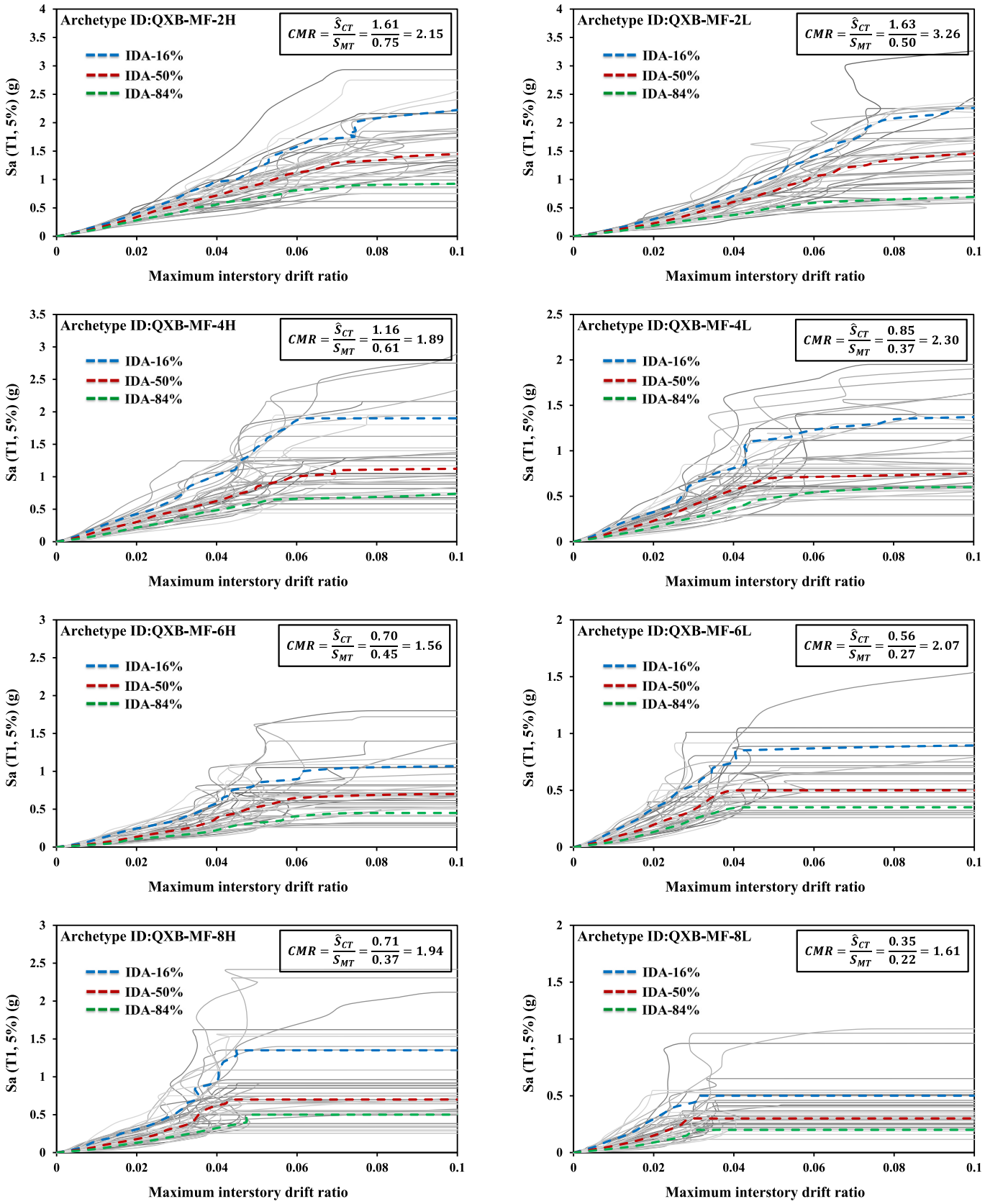

Fig. 13. IDA curves of the QXB-MF archetypes under FFGM records.

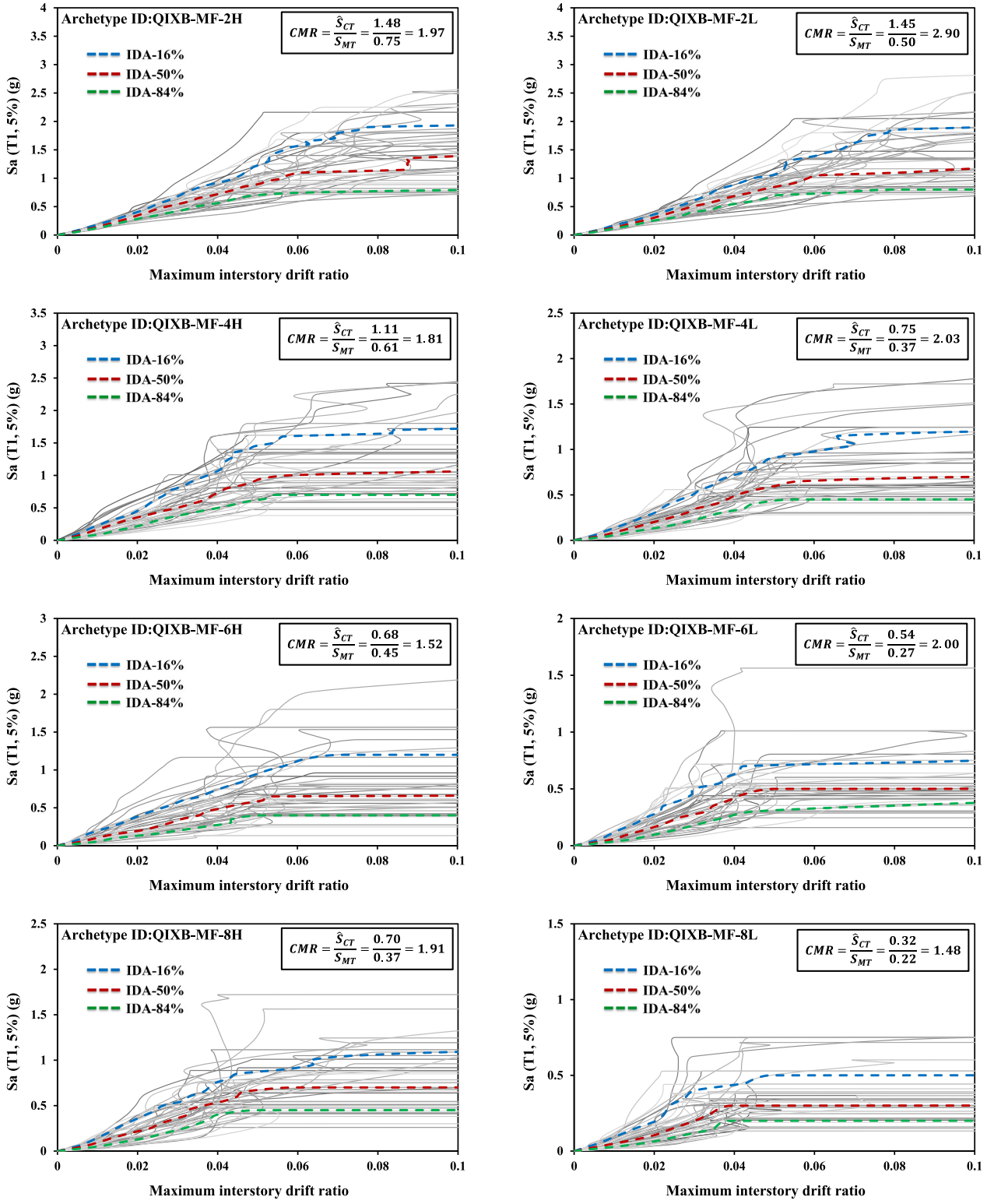

Fig. 14. IDA curves of the QIXB-MF archetypes under FFGM records.

satisfied:

$$ACMR_i \geq ACMR_{20\%} \tag{11}$$

$$\overline{ACMR_i} \geq ACMR_{10\%} \tag{12}$$

where $ACMR_i$ and $\overline{ACMR_i}$ denote the adjusted collapse margin ratio value for each archetype and the average value of the adjusted collapse margin ratio for each performance group, respectively. Additionally, the adjusted collapse margin ratio's acceptable values, $ACMR_{10\%}$ and $ACMR_{20\%}$, are determined through β_{TOT} and according to FEMA P695 [36]. Fig. 17 illustrates a juxtaposed comparison of the ACMR values for the QXB-MF and QIXB-MF archetypes. This figure illustrates that the seismic performance of the QXB-MF bracing system outperforms that of the QIXB-MF system. In addition, as the number of stories increases,

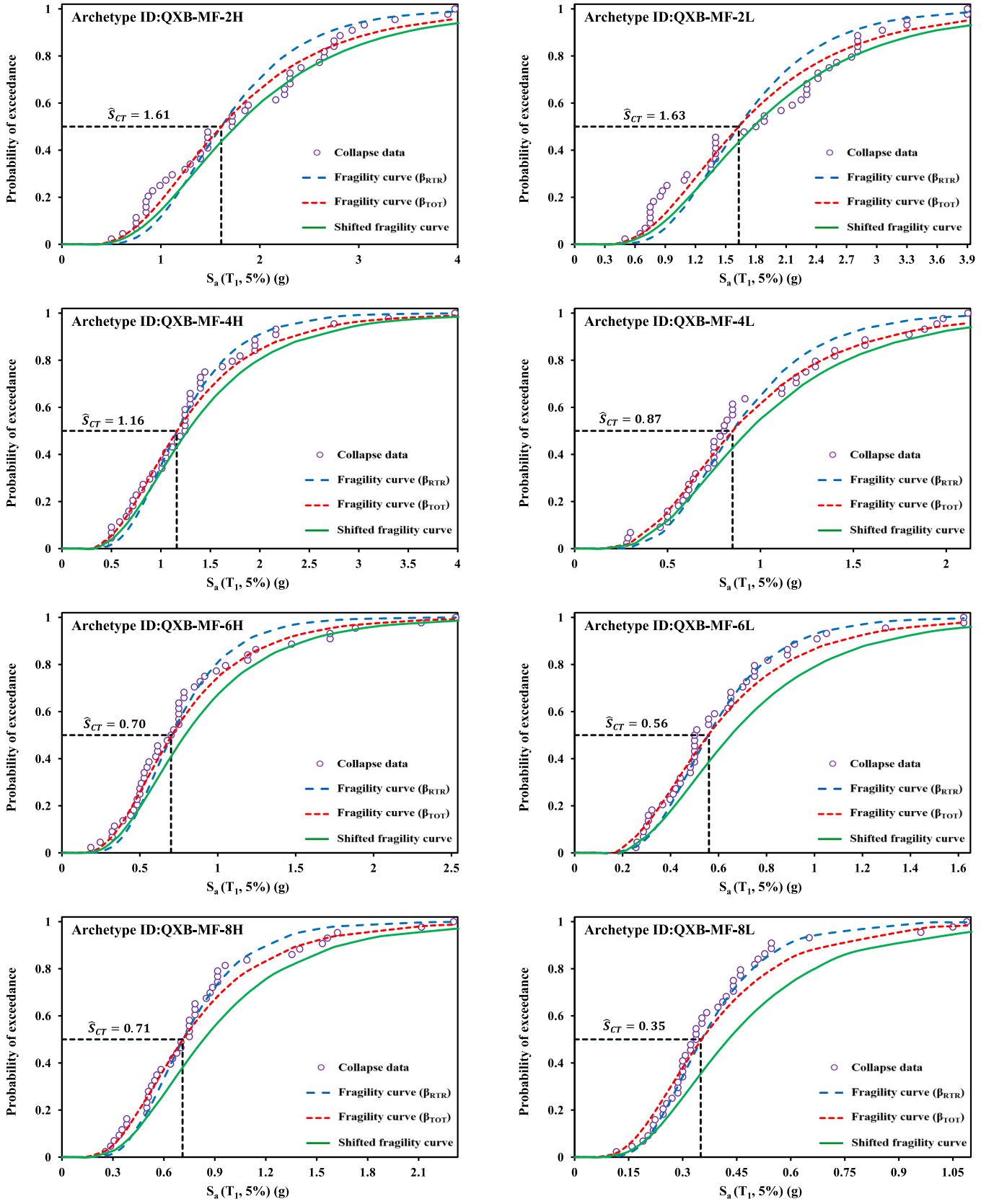

Fig. 15. Fragility curves of the QXB-MF archetypes under FFGM records.

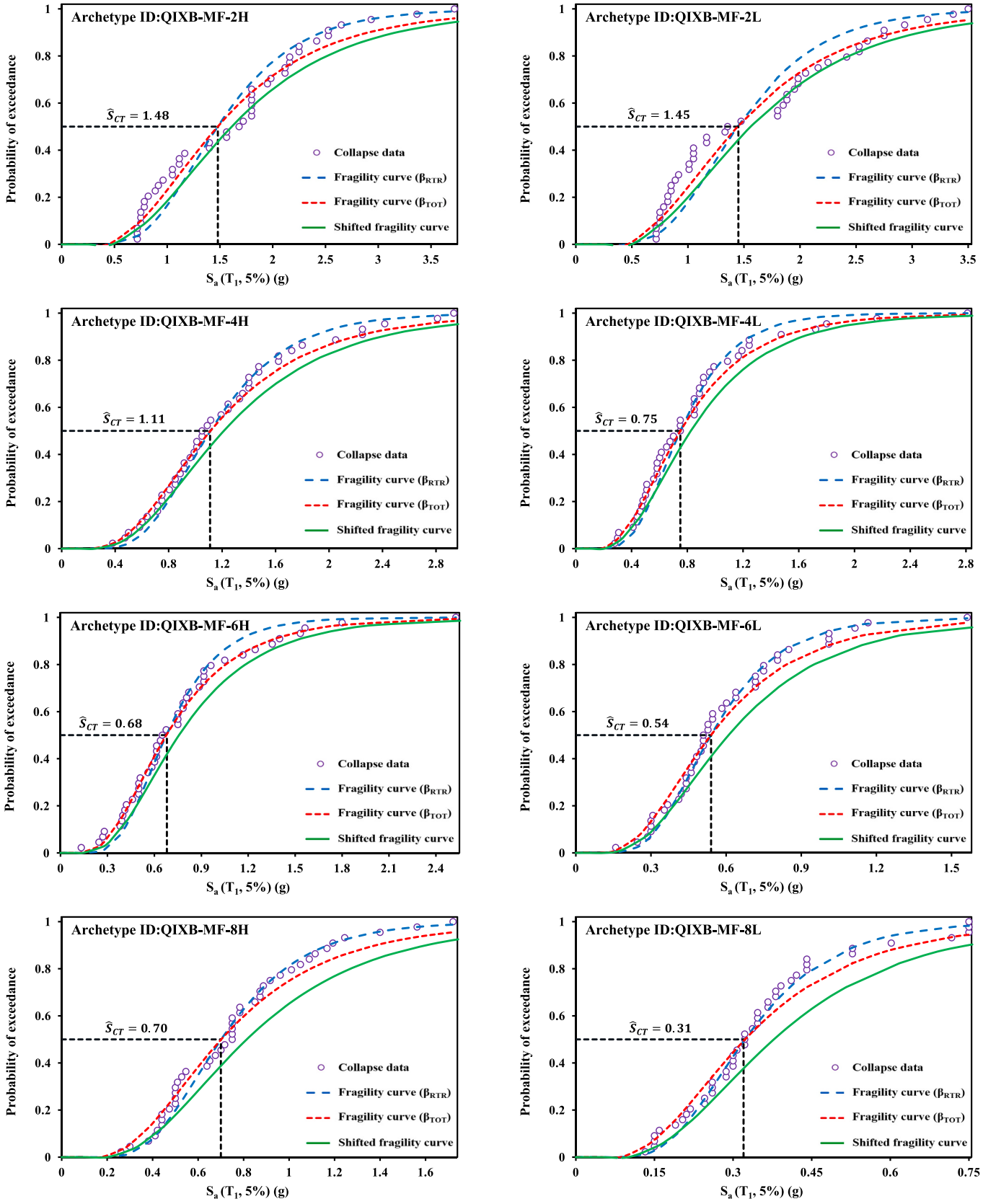

Fig. 16. Fragility curves of the QIXB-MF archetypes under FFGM records.

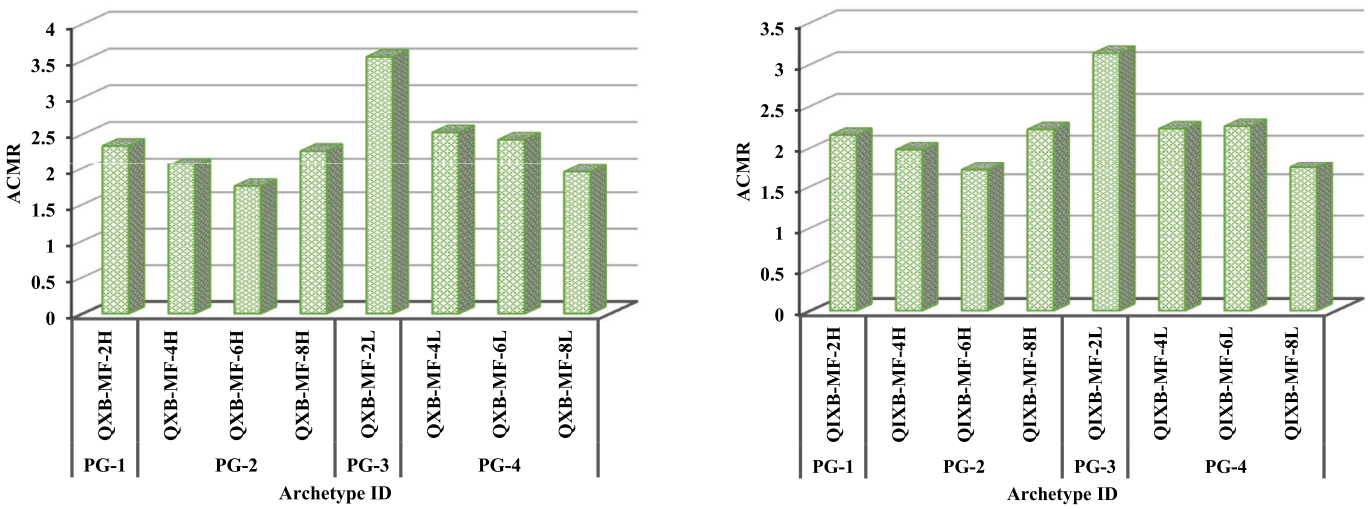

(a) (b)

Fig. 17. Comparison of the archetypes' ACMR values; (a) QXB-MF system, (b) QIXB-MF system.

Table 9
ACMRs of QXB-MF archetypes in comparison to acceptable FEMA P695 values.

PG NO.	Archetype ID	$S_{MT}(g)$	$\widehat{S}_{CT}$	*CMR*	*SSF*	*ACMR*	$ACMR_{20\%}$	$ACMR_{10\%}$	Pass/Fail
PG-1	QXB-MF-2H	0.75	1.61	2.15	1.09	2.34	1.56		Pass
	Mean of performance groupe:					2.34		1.96	Pass
PG-2	QXB-MF-4H	0.61	1.16	1.89	1.09	2.07	1.56		Pass
	QXB-MF-6H	0.45	0.70	1.56	1.12	1.75	1.56		Pass
	QXB-MF-8H	0.37	0.71	1.94	1.17	2.27	1.56		Pass
	Mean of performance groupe:					2.03		1.96	Pass
PG-3	QXB-MF-2L	0.50	1.63	3.26	1.09	3.55	1.56		Pass
	Mean of performance groupe:					3.55		1.96	Pass
PG-4	QXB-MF-4L	0.37	0.85	2.30	1.10	2.52	1.56		Pass
	QXB-MF-6L	0.27	0.56	2.07	1.17	2.42	1.56		Pass
	QXB-MF-8L	0.22	0.35	1.61	1.21	1.95	1.56		Pass
	Mean of performance groupe:					2.30		1.96	Pass

Table 10
ACMRs of QIXB-MF archetypes in comparison to acceptable FEMA P695 values.

PG NO.	Archetype ID	$S_{MT}(g)$	$\widehat{S}_{CT}$	*CMR*	*SSF*	*ACMR*	$ACMR_{20\%}$	$ACMR_{10\%}$	Pass/Fail
PG-1	QIXB-MF-2H	0.75	1.48	1.97	1.09	2.15	1.56		Pass
	Mean of performance groupe:					2.15		1.96	Pass
PG-2	QIXB-MF-4H	0.61	1.11	1.81	1.09	1.98	1.56		Pass
	QIXB-MF-6H	0.45	0.68	1.52	1.12	1.70	1.56		Pass
	QIXB-MF-8H	0.37	0.70	1.91	1.16	2.22	1.56		Pass
	Mean of performance groupe:					1.97		1.96	Pass
PG-3	QIXB-MF-2L	0.50	1.45	2.90	1.08	3.13	1.56		Pass
	Mean of performance groupe:					3.13		1.96	Pass
PG-4	QIXB-MF-4L	0.37	0.75	2.03	1.10	2.23	1.56		Pass
	QIXB-MF-6L	0.27	0.54	2.00	1.13	2.26	1.56		Pass
	QIXB-MF-8L	0.22	0.32	1.48	1.17	1.73	1.56		Pass
	Mean of performance groupe:					2.07		1.96	Pass

except for the 8-story archetype in SDC C_{max}, the ACMR value decreases. This discrepancy could be attributed to the drift control in accordance with ASCE/SEI 7–22 [42] and stronger consideration of cross-sections (particularly beams) in the 8-story archetype.

Tables 9 and 10 present the results obtained from IDA curves for the QXB-MF and QIXB-MF systems, respectively, compared to the acceptable values prescribed in FEMA P695 [36]. The outcomes indicate that both conditions outlined in Eqs. (10) and (11) have been satisfied for all QXB-MF and QIXB-MF archetypes. As a result, the presumed response modification factor $(R = 5)$ for both bracing systems is approved, and

there is no necessity to increase the R factor due to the proximity of the $\overline{ACMR}$ value of the PG-2 to $ACMR_{10\%}$ in both systems.

6.2. The over-strength factor (Ω)

In order to choose the over-strength factor (Ω) for structural systems conforming to FEMA P695 [36], the initial step involves determining the Ω factor values for performance groups based on the average of the Ω factors obtained from archetypes. Subsequently, the maximum Ω factor of the performance groups is considered, and if its value is <1/5 times the structural system's R factor and less than the number 3, it is chosen as the Ω factor of the structural system. As per FEMA P695 [36], the maximum value of the Ω factor for various performance groups should be conservatively rounded to 0.5 unit intervals and presented as the Ω factor for the system under investigation. In accordance with the pushover analysis results presented in Tables 6 and 7, it can be observed that the maximum Ω factor value for both bracing systems occurs in PG-3, with a value of 3.18. Consequently, the determined value of the over-strength factor (Ω) for both QXB-MF and QIXB-MF systems is 3.

6.3. The deflection amplification factor (C_d)

Structures designed using reduced forces must have the capacity to undergo non-elastic deformations. The maximum lateral displacement of a structure during an earthquake can be estimated by considering the enhanced elastic displacement employing the deflection amplification factor (C_d). According to FEMA P695 guidelines [36], a direct correlation exists between the C_d and R factors. In order to derive this factor, it is necessary to divide the final R factor by the B_I coefficient, as specified in Eq. (12):

$$C_d = \frac{R}{B_I} \tag{13}$$

In this equation, the B_I coefficient depends on the structural system's effective damping (β_I) under study. In general, the effective damping of structural systems is regarded as approximately 5% of critical damping. Under such conditions, as stipulated by ASCE/SEI 7–22 [42], the B_I coefficient will be assigned a value of one, leading to the equivalence of the C_d factor with the R factor. Hence, the determined value of the C_d factor for both QXB-MF and QIXB-MF systems is equal to the R factor ($C_d = 5$).

7. Conclusions

This study employs FEMA P695 methodology to determine the seismic performance factors (SPFs) of two innovative quasi-X bracing systems, called the quasi-X-braced steel moment frame (QXB-MF) and the quasi inverse-X-braced steel moment frame (QIXB-MF). To accomplish this objective, eight three-dimensional 2-, 4-, 6-, and 8-story archetypes in four performance groups were designed for each of the bracing systems in the seismic design categories (SDC) C_{min} and C_{max} based on presumed SPFs. Initially, non-linear static (pushover) analysis was conducted to compute the period-based ductility (μ_T) and over-strength factor (Ω) per archetype. Subsequently, incremental dynamic analysis (IDA) was carried out using the advanced "hunt and fill" algorithm under 44 far-field ground motion (FFGM) records to estimate the collapse capacity of archetypes and calculate the adjusted collapse margin ratio (ACMR). The accuracy of the primary SPFs was evaluated by comparing the derived ACMRs from the IDA curves with the acceptable values defined in FEMA P695. The important results of this study are as follows:

- Regarding the outcomes obtained from pushover analyses, the 2-story quasi-X bracing archetypes in both SDCs have the highest Ω factor, whereas the 8-story quasi-X bracing archetypes have the highest μ_T factor.
- Regarding the results acquired from IDA analyses, the ACMR value of quasi-X bracing archetypes decreases as the number of stories increases, except for the 8-story archetype in SDC C_{max}, because stronger cross-sections have been utilized in the design of these archetypes to control drift according to the ASCE/SEI 7–22 standard.
- Evaluating and comparing the extracted results from pushover and IDA analyses revealed that the QXB-MF bracing system surpasses the QIXB-MF system regarding seismic performance.
- The increase in the standard deviation (total uncertainty) amount for both bracing systems has led to a decrease in the slope of fragility curves and an increase in the collapse probability at MCE ground motion intensity (S_{MT}).
- The outcomes indicate that the presumed response modification factor (R) meets the criteria of FEMA P695 for both bracing systems, satisfying two conditions. Thus, the R factor of 5 is ideal for designing both QXB-MF and QIXB-MF systems.
- The maximum average over-strength factor (Ω) occurs in PG-3, with a value of 3.18. Hence, the appropriate value of the Ω factor for designing both QXB-MF and QIXB-MF systems is 3.
- If the effective damping of a system is approximately 5% of the critical damping, with regard to the equations specified in FEMA P695, the deflection amplification factor (C_d) is equal to the R factor. Therefore, the suitable value of the C_d factor for designing both QXB-MF and QIXB-MF systems is 5.

Quasi-X bracing systems, owing to their elliptical geometry, have the capability of providing not only sufficient stiffness and strength but also favorable ductility. Considering the authors' knowledge, these novel bracing systems are currently under study and have not yet been utilized in buildings. Additionally, any building code or standard has not addressed their seismic performance factors. Consequently, the present study can serve as an introduction to the seismic design of these bracing systems.

CRediT authorship contribution statement

Alireza Shirpour: Investigation, Software, Writing – original draft. **Nader Fanaie:** Conceptualization, Methodology, Supervision, Validation, Data curation, Visualization, Writing – review & editing.

Declaration of Competing Interest

The authors certify that they have no affiliations with or involvement in any organization or entity with any financial interest (such as employment, patent-licensing arrangements, etc.), or non-financial interest (such as personal or professional relationships, affiliations, knowledge or beliefs) in the subject matter discussed in this manuscript.

Data availability

Data will be made available on request.

References

[1] J. Shen, Impact of unique practice in concentrically braced frames on their seismic performance, J. Constr. Steel Res. 201 (2023) 107718, https://doi.org/10.1016/j.jcsr.2022.107718.
[2] M.S. Kumar, R. Senthilkumar, L. Sourabha, Seismic performance of special concentric steel braced frames, Structures. 20 (2019) 166–175, https://doi.org/10.1016/j.istruc.2019.03.012.
[3] M. Mahmoudi, A.Z. Mehrizi, A. Shirpour, Evaluation of the effect of end-connection specifications on lateral bearing capacity of concentrically braced steel frames, Int. J. Steel Struct. 18 (2018) 179–187, https://doi.org/10.1007/s13296-018-0314-5.
[4] R. Tabatabaei Mirhosseini, S. Hamzeh, Modified bar-fuse damper in gusset plate detail to improve seismic behavior of bracing system, Structures. 29 (2021) 954–965, https://doi.org/10.1016/j.istruc.2020.12.011.
[5] M.R. Solaimani Nezhad, M. Mahmoudi, Experimental and analytical evaluation of the seismic performance of Y-shaped braces equipped with yielding diagonal dampers, J. Build. Eng. 42 (2021), https://doi.org/10.1016/j.jobe.2021.102362.

[6] M. Bastami, R. Ahmady Jazany, Development of centrically fused braced frame (CFBF) for seismic regions, Soil Dyn. Earthq. Eng. 127 (2019) 105856, https://doi.org/10.1016/j.soildyn.2019.105856.
[7] C. Qiu, X. Du, Seismic performance of multistory CBFs with novel recentering energy dissipative braces, J. Constr. Steel Res. 168 (2020) 105864, https://doi.org/10.1016/j.jcsr.2019.105864.
[8] E. Afsar Dizaj, N. Fanaie, A. Zarifpour, Probabilistic seismic demand assessment of steel frames braced with reduced yielding segment buckling restrained braces, Adv. Struct. Eng. 21 (2018) 1002–1020, https://doi.org/10.1177/1369433217737115.
[9] R.G. Tyler, Further notes on a steel energy-absorbing element for braced frameworks, Bull. N. Z. Soc. Earthq. Eng. 18 (1985) 270–279.
[10] D. Jurukovski, M. Petkovski, Z. Rakicevic, Energy absorbing elements in regular and composite steel frame structures, Eng. Struct. 17 (1995) 319–333.
[11] V. Ciampi, A.S. Ferretti, Energy dissipation in buildings using special bracing systems, in: Proc. 10th Int. Earthq. Conf, 1990.
[12] A.S. Pall, C. Marsh, Response of friction damped braced frames, J. Struct. Div. 108 (1982) 1313–1323.
[13] A. Vulcano, Design of damped steel bracing systems for seismic control of framed structures, in: Procs. 10th Eur. Conf. Earthq. Eng, 1994, pp. 1567–1572.
[14] V. Ciampi, V. Paolone, M. De Angelis, On the seismic design of dissipative bracings, in: Memorias, Tenth World Conf. Earthq. Eng, 1992, pp. 4133–4138.
[15] V. Ciampi, M. Arcangeli, R. Ferlito, Dissipative bracings for seismic protection of buildings, in: Proc. Int. Meet. Earthq. Prot. Build, 1991, pp. 87–100.
[16] S. Sabouri-Ghomi, A. Roufegarinejad, Non-linear behavior of yielding damped braced frames, Struct. Des. Tall Spec. Build. 14 (2005) 37–45.
[17] B. Payandehjoo, S. Sabouri-Ghomi, P. Ebadi, Seismic behavior of X-shaped drawer bracing system (DBS) and X-braced frames with heavy central Core, J. Earthq. Tsunami 10 (2016) 1–28, https://doi.org/10.1142/S1793431116500044.
[18] S.B. Beheshti-Aval, H. Mahbanouei, F. Zareian, A hybrid friction-yielding damper to equip concentrically braced steel frames, Int. J. Steel Struct. 13 (2013) 577–587.
[19] Z. Andalib, M.A. Kafi, A. Kheyroddin, M. Bazzaz, Experimental investigation of the ductility and performance of steel rings constructed from plates, J. Constr. Steel Res. 103 (2014) 77–88, https://doi.org/10.1016/j.jcsr.2014.07.016.
[20] T. Trombetti, S. Silvestri, G. Gasparini, I. Ricci, Stiffness-strength-ductility-design approaches for crescent shaped braces, Open Constr. Build. Technol. J. 3 (2009) 127–140, https://doi.org/10.2174/1874836800903020127.
[21] M. Palermo, S. Silvestri, G. Gasparini, T. Trombetti, Crescent shaped braces for the seismic design of building structures, Mater. Struct. Constr. 48 (2015) 1485–1502, https://doi.org/10.1617/s11527-014-0249-z.
[22] M. Palermo, L. Pieraccini, A. Dib, S. Silvestri, T. Trombetti, Experimental tests on crescent shaped braces hysteretic devices, Eng. Struct. 144 (2017) 185–200, https://doi.org/10.1016/j.engstruct.2017.04.034.
[23] O. Kammouh, S. Silvestri, M. Palermo, G.P. Cimellaro, Performance-based seismic design of multistory frame structures equipped with crescent-shaped brace, Struct. Control. Health Monit. 25 (2018), e2079.
[24] M. Palermo, V. Laghi, G. Gasparini, S. Silvestri, T. Trombetti, Analytical estimation of the key performance points of the tensile force-displacement response of crescent shaped braces, Soil Dyn. Earthq. Eng. 148 (2021) 106839, https://doi.org/10.1016/j.soildyn.2021.106839.
[25] E. Mokhtari, V. Laghi, M. Palermo, S. Silvestri, Quasi-static cyclic tests on a half-scaled two-storey steel frame equipped with crescent shaped braces, Eng. Struct. 232 (2021) 111836, https://doi.org/10.1016/j.engstruct.2020.111836.
[26] M. Boostani, O. Rezaifar, M. Gholhaki, Introduction and seismic performance investigation of the proposed lateral bracing system called “OGrid”, Arch. Civ. Mech. Eng. 18 (2018) 1024–1041, https://doi.org/10.1016/j.acme.2018.02.003.
[27] M. Boostani, O. Rezaifar, M. Gholhaki, Seismic performance investigation of new lateral bracing system called “OGrid-H”, SN Appl. Sci. 1 (2019) 1–24, https://doi.org/10.1007/s42452-019-0369-8.
[28] H.G. Jouneghani, A. Haghollahi, Experimental study on hysteretic behavior of steel moment frame equipped with elliptical brace, Steel Compos. Struct. 34 (2020) 891–907, https://doi.org/10.12989/scs.2020.34.6.891.
[29] A. Shamivand, J. Akbari, Ring-shaped lateral bracing system for steel structures, Int. J. Steel Struct. 20 (2020) 493–503, https://doi.org/10.1007/s13296-019-00299-z.
[30] M. Ismail, An elastoplastic bracing system for structural vibration control, Eng. Struct. 200 (2019) 109671, https://doi.org/10.1016/j.engstruct.2019.109671.
[31] N. Fanaie, A. Shirpour, Analytical and numerical evaluation of quarter-elliptic-braced steel moment frames (QEB-MFs), Structures. 49 (2023) 426–442, https://doi.org/10.1016/j.istruc.2023.01.100.
[32] M. Mahmoudi, M. Zaree, Evaluating response modification factors of concentrically braced steel frames, J. Constr. Steel Res. 66 (2010) 1196–1204, https://doi.org/10.1016/j.jcsr.2010.04.004.
[33] N. Fanaie, S. Ezzatshoar, Studying the seismic behavior of gate braced frames by incremental dynamic analysis (IDA), J. Constr. Steel Res. 99 (2014) 111–120, https://doi.org/10.1016/j.jcsr.2014.04.008.
[34] N. Fanaie, E.A. Dizaj, Response modification factor of the frames braced with reduced yielding segment BRB, Struct. Eng. Mech. 50 (2014) 1–17, https://doi.org/10.12989/sem.2014.50.1.001.
[35] N. Fanaie, S.O. Shamlou, Response modification factor of mixed structures, Steel Compos. Struct. 19 (2015) 1449–1466, https://doi.org/10.12989/scs.2015.19.6.1449.
[36] FEMA, P695, Quantification of Building Seismic Performance Factors, 2009.
[37] N. Mashhadiali, A. Kheyroddin, Quantification of the seismic performance factors of steel hexagrid structures, J. Constr. Steel Res. 157 (2019) 82–92, https://doi.org/10.1016/j.jcsr.2019.02.013.
[38] F.R. Rofooei, A. Seyedkazemi, Evaluation of the Seismic Performance Factors for Steel Diagrid Structural Systems Using FEMA P-695 and ATC-19 Procedures, Springer Netherlands, 2020, https://doi.org/10.1007/s10518-020-00876-2.
[39] M. Ghasemi, N. Fanaie, H. Khorshidi, Seismic performance factors of a dual system with IMRF and cable-cylinder bracing, J. Build. Eng. 39 (2021) 102309, https://doi.org/10.1016/j.jobe.2021.102309.
[40] M. Mahmoudi, A. Shirpour, A. Zarezadeh, The effects of mid-span connection specifications on compressive performance of cross (X) braces, Int. J. Steel Struct. 19 (2019) 1125–1133, https://doi.org/10.1007/s13296-018-0192-x.
[41] EN 1993-1-1, Eurocode 3: Design of Steel Structures - Part 1–1: General Rules and Rules for Buildings, European Committee for Standardisation, Brussels, 2005.
[42] ASCE/SEI 7-22, Minimum Design Loads and Associated Criteria for Buildings and Other Structures, 2022.
[43] ANSI/AISC 360-16, Specification for Structural Steel buildings, 2016.
[44] ANSI/AISC 341–16, Seismic Provisions for Structural Steel Buildings, 2016, https://doi.org/10.1201/b11248-8.
[45] S. Mazzoni, F. McKenna, M.H. Scott, G.L. Fenves, OpenSees Command Language Manual, 2007.
[46] E. Karamanci, D.G. Lignos, Computational approach for collapse assessment of concentrically braced frames in seismic regions, J. Struct. Eng. 140 (2014), https://doi.org/10.1061/(asce)st.1943-541x.0001011.
[47] D.G. Lignos, H. Krawinkler, A steel database for component deterioration of tubular hollow square steel columns under varying axial load for collapse assessment of steel structures under earthquakes, in: Proc. 7th Int. Conf. Urban Earthq. Eng, 2010.
[48] D.G. Lignos, H. Krawinkler, Deterioration modeling of steel components in support of collapse prediction of steel moment frames under earthquake loading, J. Struct. Eng. 137 (2011) 1291.
[49] D.G. Lignos, M. Asce, A.R. Hartloper, S.M. Asce, A. Elkady, A.M. Asce, G. G. Deierlein, F. Asce, R. Hamburger, F. Asce, Proposed Updates to the ASCE 41 Nonlinear Modeling Parameters for Wide-Flange Steel Columns in Support of Performance-Based Seismic Engineering 145, 2019, pp. 1–13, https://doi.org/10.1061/(ASCE)ST.1943-541X.0002353.
[50] NIST 2017b, Guidelines for Nonlinear Structural Analysis for Design of Buildings Part IIa–Steel Moment Frames, 2017, https://doi.org/10.6028/NIST.GCR.17-917-46v2.
[51] A. Gupta, H. Krawinkler, Seismic Demands for Performance Evaluation of Steel Moment Resisting Frame Structures, 1999.
[52] ATC-24, Guidelines for Cyclic Seismic Testing of Components of Steel Structures, 1992.
[53] ASCE/SEI 41-06, Seismic Rehabilitation of Existing Buildings, 2006, https://doi.org/10.1126/science.1.3.84.
[54] D. Vamvatsikos, C.A. Cornell, Incremental dynamic analysis, Earthq. Eng. Struct. Dyn. 31 (2002) 491–514, https://doi.org/10.1002/eqe.141.
[55] J.W. Baker, C.A. Cornell, Spectral shape, epsilon and record selection, Earthq. Eng. Struct. Dyn. 35 (2006) 1077–1095, https://doi.org/10.1002/eqe.571.
[56] C.B. Haselton, J.W. Baker, A.B. Liel, G.G. Deierlein, Accounting for ground-motion spectral shape characteristics in structural collapse assessment through an adjustment for epsilon, J. Struct. Eng. 137 (2011) 332–344, https://doi.org/10.1061/(asce)st.1943-541x.0000103.